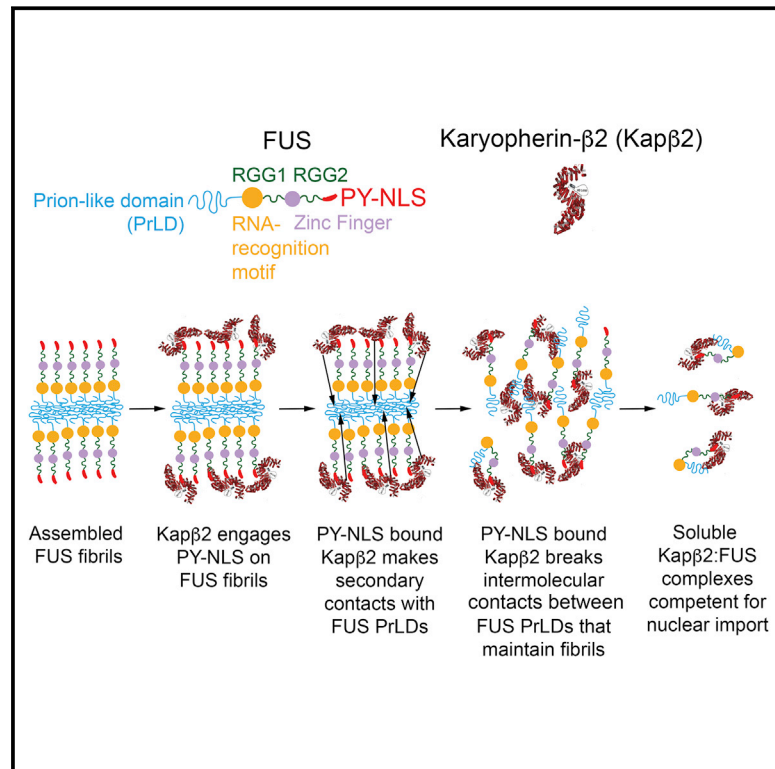# Nuclear-Import Receptors Reverse Aberrant Phase Transitions of RNA-Binding Proteins with Prion-like Domains

Graphical Abstract

Authors

Lin Guo, Hong Joo Kim, Hejia Wang, ..., Yuh Min Chook, J. Paul Taylor, James Shorter

Correspondence

jpaul.taylor@stjude.org (J.P.T.), jshorter@pennmedicine.upenn.edu (J.S.)

In Brief

Nuclear-import receptors can reverse phase separation and aggregation of proteins with prion-like domains, including FUS and TDP-43, to mitigate neurodegeneration *in vivo*.

Highlights

- Nuclear-localization sequences (NLSs) are disaggregation signals in the cytoplasm

- Nuclear-import receptors (NIRs) disaggregate NLS-bearing cargo in the cytoplasm

- NIRs reverse phase separation by RNA-binding proteins with prion-like domains

- NIRs rescue degeneration caused by disease-linked FUS and hnRNPA2 *in vivo*

Nuclear-Import Receptors Reverse Aberrant Phase Transitions of RNA-Binding Proteins with Prion-like Domains

Lin Guo,[1,13] Hong Joo Kim,[2,13] Hejia Wang,[1,13] John Monaghan,[3,12,14] Fernande Freyermuth,[4,5,14] Julie C. Sung,[1,14] Kevin O'Donovan,[2] Charlotte M. Fare,[1] Zamia Diaz,[1] Nikita Singh,[1] Zi Chao Zhang,[6,7] Maura Coughlin,[2] Elizabeth A. Sweeny,[1] Morgan E. DeSantis,[1] Meredith E. Jackrel,[1] Christopher B. Rodell,[8] Jason A. Burdick,[8] Oliver D. King,[9] Aaron D. Gitler,[10] Clotilde Lagier-Tourenne,[4,5] Udai Bhan Pandey,[3] Yuh Min Chook,[6] J. Paul Taylor,[2,11,*] and James Shorter[1,15,*]

[1]Department of Biochemistry and Biophysics, Perelman School of Medicine, University of Pennsylvania, Philadelphia, PA 19104, USA
[2]Department of Cell and Molecular Biology, St. Jude Children's Research Hospital, Memphis, TN 38120, USA
[3]Department of Pediatrics, Child Neurology and Neurobiology, Children's Hospital of Pittsburgh, University of Pittsburgh, Pittsburgh, PA 15224, USA
[4]Department of Neurology, Massachusetts General Hospital, Harvard Medical School, Boston, MA 02114, USA
[5]Broad Institute of Harvard University and MIT, Cambridge, MA 02142, USA
[6]Department of Pharmacology, University of Texas Southwestern Medical Center, Dallas, TX 75390, USA
[7]Institute of Life Sciences, Southeast University, Nanjing, 210096 Jiangsu, China
[8]Department of Bioengineering, University of Pennsylvania, Philadelphia, PA 19104, USA
[9]Department of Neurology, University of Massachusetts Medical School, Worcester, MA 01655, USA
[10]Department of Genetics, Stanford University School of Medicine, Stanford, CA 94305, USA
[11]Howard Hughes Medical Institute, Chevy Chase, MD 20815, USA
[12]Present address: School of Medicine, Trinity College Dublin, Dublin, Ireland
[13]These authors contributed equally
[14]These authors contributed equally
[15]Lead Contact
*Correspondence: jpaul.taylor@stjude.org (J.P.T.), jshorter@pennmedicine.upenn.edu (J.S.)
https://doi.org/10.1016/j.cell.2018.03.002

SUMMARY

RNA-binding proteins (RBPs) with prion-like domains (PrLDs) phase transition to functional liquids, which can mature into aberrant hydrogels composed of pathological fibrils that underpin fatal neurodegenerative disorders. Several nuclear RBPs with PrLDs, including TDP-43, FUS, hnRNPA1, and hnRNPA2, mislocalize to cytoplasmic inclusions in neurodegenerative disorders, and mutations in their PrLDs can accelerate fibrillization and cause disease. Here, we establish that nuclear-import receptors (NIRs) specifically chaperone and potently disaggregate wild-type and disease-linked RBPs bearing a NLS. Karyopherin-β2 (also called Transportin-1) engages PY-NLSs to inhibit and reverse FUS, TAF15, EWSR1, hnRNPA1, and hnRNPA2 fibrillization, whereas Importin-α plus Karyopherin-β1 prevent and reverse TDP-43 fibrillization. Remarkably, Karyopherin-β2 dissolves phase-separated liquids and aberrant fibrillar hydrogels formed by FUS and hnRNPA1. *In vivo*, Karyopherin-β2 prevents RBPs with PY-NLSs accumulating in stress granules, restores nuclear RBP localization and function, and rescues degeneration caused by disease-linked FUS and hnRNPA2. Thus, NIRs therapeutically restore RBP homeostasis and mitigate neurodegeneration.

INTRODUCTION

There are no effective therapies for several fatal neurodegenerative disorders, including amyotrophic lateral sclerosis (ALS), frontotemporal dementia (FTD), and multisystem proteinopathy (MSP) in which specific RNA-binding proteins (RBPs) with prion-like domains (PrLDs) mislocalize and aggregate in the cytoplasm of degenerating cells (Harrison and Shorter, 2017). For example, wild-type (WT) or mutant FUS, TAF15, and EWSR1 are depleted from the nucleus and form cytoplasmic aggregates in degenerating neurons in some ALS/FTD cases, whereas in MSP, WT, or mutant hnRNPA1 and hnRNPA2 exhibit this phenotype in degenerating tissues, including muscle, brain, and bone (Harrison and Shorter, 2017). For these RBPs with a PY-nuclear localization signal (NLS) (Lee et al., 2006), as well as TDP-43, which harbors a canonical NLS (cNLS) (Figure 1A), a major pathological event is mislocalization from the nucleus to cytoplasmic aggregates (Harrison and Shorter, 2017). Indeed, defects in nuclear transport contribute to ALS, FTD, and MSP (Chou et al., 2018; Kim and Taylor, 2017).

PrLDs possess a low-complexity, amino-acid composition similar to prion domains (PrDs), which enable certain yeast proteins (e.g., Sup35) to form prions (March et al., 2016). PrDs and

(legend on next page)

PrLDs are enriched in Gly and uncharged polar amino acids, including Gln, Asn, Tyr, and Ser. PrDs of yeast proteins enable beneficial liquid-liquid phase separation (LLPS) and prionogenesis (Franzmann et al., 2018; March et al., 2016). PrLDs of human RBPs drive their pathological aggregation and disease-linked mutations in PrLDs can accelerate aggregation (March et al., 2016). However, PrLDs in human RBPs also play important roles in functional protein-protein interactions and drive LLPS events that underpin biogenesis of functional membraneless organelles, including stress granules (SGs) and nuclear paraspeckles (March et al., 2016). Thus, PrLDs switch from intrinsically unfolded states in monodisperse solution to condensed multimeric liquid phases in which PrLDs retain disordered character. These liquid compartments exhibit rapid internal dynamics and are sustained by transient, multivalent intermolecular contacts between PrLDs and between PrLDs and other RBP domains (Monahan et al., 2017). RBP liquids can mature into solid hydrogels comprised of stable fibrils maintained by intermolecular cross-β contacts between PrLDs (Molliex et al., 2015; Murakami et al., 2015; Patel et al., 2015). Disease-linked mutations in PrLDs (e.g., hnRNPA1^{D262V}) accelerate fibrillization and aberrant phase transitions to the solid state (Kim et al., 2013; Molliex et al., 2015; Murakami et al., 2015; Patel et al., 2015). These aberrant solid, gel-like phases of RBPs with PrLDs are closely tied to neurodegeneration (Harrison and Shorter, 2017).

Agents that reverse fibrillization and aberrant phase transitions of RBPs with PrLDs while simultaneously restoring their functionality and nuclear localization could mitigate neurodegeneration by eradicating: (1) any toxic gain of function of misfolded species, and (2) any loss of function due to sequestration in cytoplasmic aggregates (Shorter, 2016). Previously, we engineered a protein disaggregase from yeast, Hsp104, to rapidly disaggregate TDP-43 and FUS fibrils linked to ALS/FTD (Shorter, 2016). However, metazoa lack Hsp104. Whether metazoa harbor machinery that disaggregates fibrils and deleterious hydrogels formed by RBPs with PrLDs is unknown. Here, we establish that nuclear-import receptors (NIRs) prevent and reverse fibrillization of RBPs with an NLS. Elevating NIR expression prevents RBPs with PrLDs accumulating in SGs, restores nuclear RBP localization and function, and rescues degeneration caused by disease-linked RBPs. Thus, NIRs could therapeutically restore RBP homeostasis in ALS, FTD, MSP, and other deadly neurodegenerative disorders.

RESULTS

Karyopherin-β2 Is a Molecular Chaperone for RBPs with a PY-NLS

NIRs bind NLSs tightly and break hydrophobic contacts between FG-repeat-rich nucleoporins as they traverse the nuclear pore during nuclear transport (Schmidt and Görlich, 2016). Thus, we reasoned that NIRs might also bind to the NLSs of RBPs with PrLDs and disrupt intermolecular contacts between PrLDs to antagonize pathological fibrillization. To assess this possibility, we used pure RBP fibrillization assays. Here, RBPs are purified with an N-terminal GST tag, which can be selectively removed by TEV protease to elicit rapid assembly of RBP fibrils that bear close ultrastructural resemblance to those that accumulate in disease (Couthouis et al., 2011, 2012; Johnson et al., 2009; Kim et al., 2013; Sun et al., 2011). Under our conditions, RBPs rapidly fibrillize and do not form macroscopic liquid droplets. Thus, we can assess NIR activity under conditions where fibrillization is the dominant pathway.

We assessed spontaneous FUS, TAF15, EWSR1, hnRNPA1, and hnRNPA2 fibrillization (i.e., in the absence of preformed fibrils) in the absence or presence of their specific NIR, Karyopherin-β2 (Kapβ2, also called Transportin-1 or Importin-β2) (Lee et al., 2006). As negative controls, we used Kapβ2$^{W460A:W730A}$ and Importin-α (Impα) plus Karyopherin-β1 (Kapβ1), which unlike Kapβ2, do not bind the PY-NLS of these RBPs (Lee et al., 2006). Kapβ2 strongly inhibited FUS, TAF15, EWSR1, hnRNPA1, and hnRNPA2 fibrillization, whereas Kapβ2$^{W460A:W730A}$ or Impα and Kapβ1 did not (Figures 1B, 1C, and S1A). The half maximal inhibitory concentration (IC$_{50}$) was ~1–2 μM for each RBP (Figure 1D). Deleting the PY-NLS from FUS, TAF15, EWSR1, hnRNPA1, and hnRNPA2 did not affect fibrillization but diminished inhibition by Kapβ2 (Figures 1B and S1A). Thus, Kapβ2 is a molecular chaperone for RBPs with a PY-NLS.

The hnRNPA1 and hnRNPA2 PY-NLSs are immediately C-terminal to a hexapeptide in their PrLDs (residues 259–264 in hnRNPA1 and 287–292 in hnRNPA2), which is critical for fibrillization (Figure 1A). Deletion of this hexapeptide prevents

Figure 1. Kapβ2 Is a Molecular Chaperone for Diverse RBPs with a PY-NLS
(A) Domain architecture of FUS, TAF15, EWSR1, hnRNPA1, hnRNPA2, and TDP-43. Disease-linked mutations used in this study and domains are indicated: PrLD (blue), Gly-rich domain (mauve), RRM (yellow), RGG (green), Zinc finger (gray), and NLS (salmon).
(B) FUS, FUS^{ΔNLS}, TAF15, TAF15^{ΔNLS}, EWSR1, EWSR1^{ΔNLS}, hnRNPA1, hnRNPA1^{ΔNLS}, hnRNPA2, or hnRNPA2^{ΔNLS} (5 μM) were incubated with buffer, Kapβ2 (5 μM), Kapβ2$^{W460A:W730A}$ (5 μM), or Impα (5 μM) plus Kapβ1 (5 μM). Fibrillization was assessed by sedimentation. Values are means ± SEM (n = 3).
(C) Fibrillization reactions performed as in (B) and processed for EM. Arrows denote fibrils. Scale bar, 0.5 μm.
(D) Kapβ2 IC$_{50}$s for fibrillization of indicated RBPs (5 μM) performed as in (B). IC$_{50}$ for FUS^{R495X} could not be determined and is >20 μM.
(E) FUS (5 μM) was incubated with buffer, Kapβ2 (5 μM), HDAC1 (5 μM or 50 μM), or anti-FUS antibody (5 μM). Fibrillization was assessed by sedimentation. Values are means ± SEM (n = 3).
(F) FUS, TAF15, hnRNPA1, or hnRNPA2 (5μM) were incubated as in (B) in the absence or presence of Kapβ2 (5 μM) plus or minus Ran^{GDP} or Ran^{GTP} (25 μM). Fibrillization was assessed by sedimentation. Values are means ± SEM (n = 3).
(G) FUS^{R234L}, FUS^{R495X}, FUS^{H517Q}, FUS^{R521C}, FUS^{R521H}, FUS^{P525L}, TAF15^{G391E}, TAF15^{R408C}, EWSR1^{G511A}, EWSR1^{P552L}, hnRNPA1^{D262V}, hnRNPA1^{D262N}, or hnRNPA2^{D290V} (5 μM) were incubated as in (B) with buffer, Kapβ2 (5 μM), or Kapβ2$^{W460A:W730A}$ (5 μM). Fibrillization was assessed by sedimentation. Values are means ± SEM (n = 3).
(H) TDP-43, TDP-43^{Q331K}, TDP-43$^{188–414}$, or TDP-43^{ΔNLS} (5 μM) were incubated with buffer Kapβ2 (5 μM) or Impα (5 μM) plus Kapβ1 (5 μM). Fibrillization was assessed by sedimentation. Values are means ± SEM (n = 3).
See also Figure S1.

hnRNPA1 and hnRNPA2 fibrillization (Kim et al., 2013). Kapβ2 binding close to this region would prevent cross-β contacts between PrLDs that drive fibrillization. By contrast, the PY-NLS of FUS, EWSR1, and TAF15 is at the C-terminal end, distal to the N-terminal PrLD that drives fibrillization (Figure 1A). Thus, could other FUS-binding proteins inhibit fibrillization? An anti-FUS antibody that recognizes the FUS PY-NLS did not inhibit FUS fibrillization (Figures 1E and S1B), and neither did HDAC1 (Figures 1E and S1B), which binds to the FUS Gly-rich domain (residues 156–262) and C-terminal region (residues 450–526) (Wang et al., 2013). Thus, FUS fibrillization is not inhibited by any FUS-binding protein, whereas Kapβ2 engages the FUS PY-NLS to abolish FUS fibrillization.

Kapβ2 binds the PY-NLS of cargo in the cytoplasm and transports cargo across the nuclear pore to the nucleus. A small GTPase, Ran, regulates Kapβ2-cargo interactions and nuclear-transport directionality via its GTPase cycle. Ran^{GDP} is concentrated in the cytoplasm and allows Kapβ2-cargo interactions, whereas Ran^{GTP} is concentrated in the nucleus and dissociates Kapβ2 from cargo upon arrival in the nucleus (Kim and Taylor, 2017). Neither Ran^{GTP} nor Ran^{GDP} affected RBP fibrillization (Figures 1F and S1C). However, Ran^{GTP} but not Ran^{GDP} reduced the ability of Kapβ2 to inhibit FUS, TAF15, EWSR1, hnRNPA1, and hnRNPA2 fibrillization (Figures 1F and S1C). Thus, Kapβ2 chaperone activity is likely restricted to the cytoplasm.

Kapβ2 Is a Molecular Chaperone for Disease-Linked Mutant RBPs with a PY-NLS

Two ALS-linked FUS variants, FUS^{R495X} and FUS^{P525L}, cause aggressive juvenile ALS (Harrison and Shorter, 2017). The PY-NLS is deleted in FUS^{R495X} (Figure 1A), and the critical Pro of the PY-NLS is mutated to Leu in FUS^{P525L}, which reduces binding to Kapβ2 (Zhang and Chook, 2012). Nonetheless, Kapβ2 reduced FUS^{P525L} aggregation by ~50% (Figures 1G and S1D), although the IC$_{50}$ was elevated ~3.7-fold (Figure 1D). Kapβ2 had limited activity against FUS^{R495X} (Figures 1D, 1G, and S1D). By contrast, Kapβ2 abolished fibrillization of the disease-linked RBP variants: FUS^{R234L}, FUS^{H517Q}, FUS^{R521C}, FUS^{R521H}, TAF15^{G391E}, TAF15^{R408C}, EWSR1^{G511A}, EWSR1^{P552L}, hnRNPA1^{D262V}, hnRNPA1^{D262N}, and hnRNPA2^{D290V} (Figure 1G) (Harrison and Shorter, 2017). These included ALS-linked FUS variants with mutations in the PY-NLS (H517Q, R521C, and R521H), which do not reduce Kapβ2 binding as much as P525L (Zhang and Chook, 2012). Thus, Kapβ2 chaperones diverse disease-linked mutant RBPs.

NIRs Prevent TDP-43 Fibrillization

TDP-43 lacks a PY-NLS but harbors a cNLS that is decoded by Impα. Impα is then bound by Kapβ1 and transported to the nucleus (Nishimura et al., 2010). Kapβ2 does not bind the TDP-43 cNLS and does not affect spontaneous fibrillization of TDP-43 or ALS-linked TDP-43^{Q331K} (Figures 1C, 1H, and S1E). Conversely, Impα plus Kapβ1 abolished TDP-43 and TDP-43^{Q331K} fibrillization (Figures 1C, 1H, and S1E). A fibrillogenic TDP-43 fragment, TDP-43$^{188–414}$, and TDP-43$^{Δ79–98}$, which lack the cNLS, resisted inhibition by Impα plus Kapβ1 (Figures 1H and S1E). Ran^{GTP} but not Ran^{GDP} reduced inhibition of TDP-43 fibrillization by Impα plus Kapβ1 (Figure S1F). The

TDP-43 cNLS is distant from the fibrillogenic PrLD (Figure 1A), which might indicate an allosteric inhibitory effect upon NIR binding. We suggest that elevating NIR expression could block nucleation of pathological fibrils and disease onset.

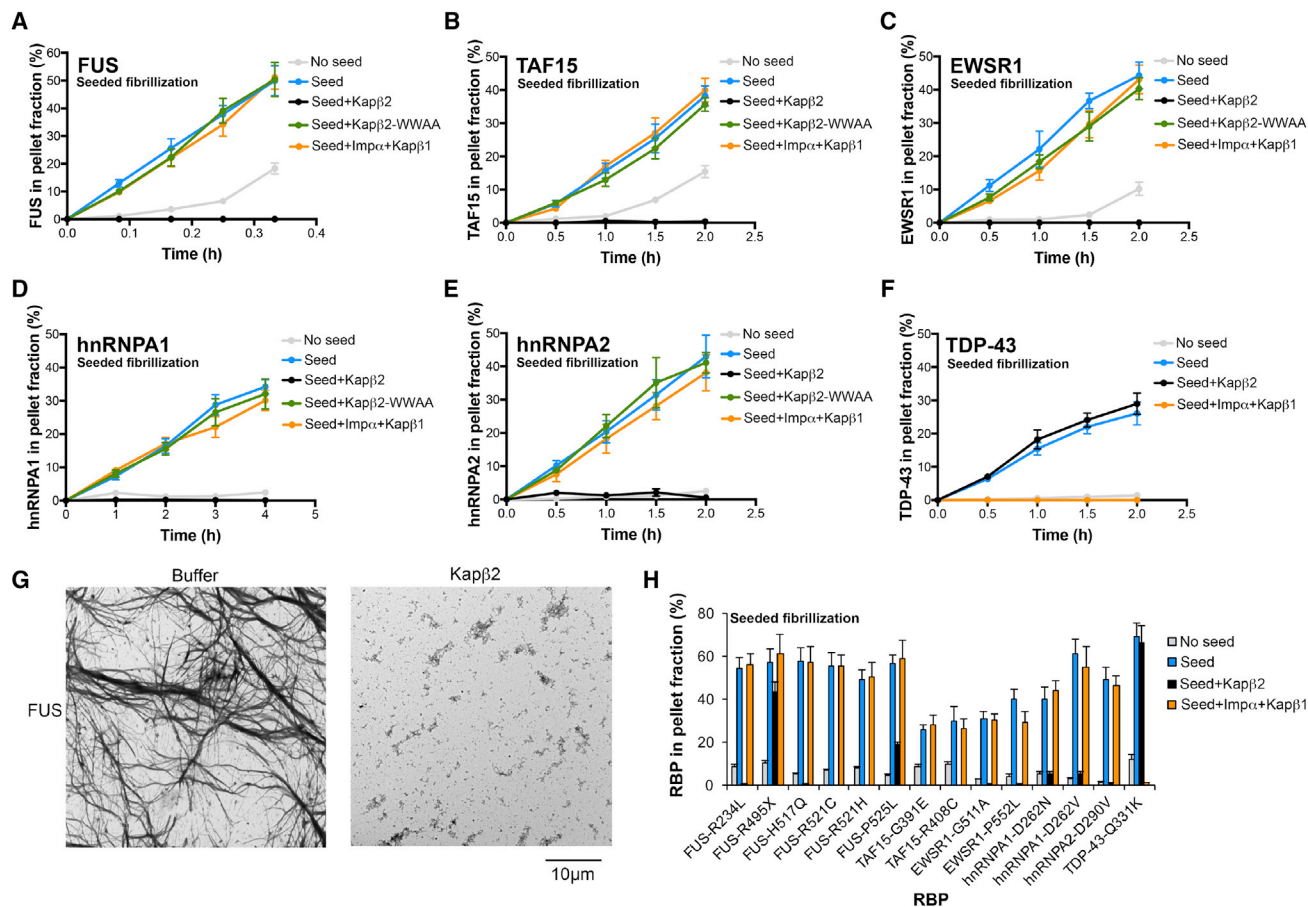### Kapβ2 Inhibits Seeded Fibrillization of Diverse RBPs with a PY-NLS

In ALS/FTD, disease pathology spreads between contiguous brain regions. Spreading may be due to transmission of self-templating, prion-like fibrils from cell to cell. Once a self-templating fibril gains access to a new cell, it converts soluble protein to the fibrillar form (March et al., 2016). Agents that prevent self-templating could halt disease progression. Could Kapβ2 inhibit RBP fibrillization seeded by preformed fibrils? For each RBP, we employed conditions wherein minimal fibrillization occurred in the absence of fibril seeds (Figures 2A–2F and S2A–S2D). Kapβ2 abolished seeded fibrillization of FUS, TAF15, EWSR1, hnRNPA1, and hnRNPA2, whereas Kapβ2$^{W460A:W730A}$ and Impα plus Kapβ1 had no effect (Figures 2A–2G and S2A–S2D). This inhibition extended to diverse disease-linked RBP variants except for the PY-NLS mutants FUS^{R495X} and FUS^{P525L} (Figures 2H and S2E). Kapβ2 did not prevent seeded TDP-43 fibrillization (Figures 2F and S2D). However, Impα and Kapβ1 abolished seeded fibrillization of TDP-43 and TDP-43^{Q331K} (Figures 2F, 2H, S2D, and S2E). Thus, NIRs could be utilized to prevent prion-like spread of self-seeding conformers during ALS, FTD, and MSP progression.

Kapβ2 Rapidly Disaggregates FUS, TAF15, and EWSR1 Fibrils

Therapeutic agents may also need to clear fibrils rather than simply impede their assembly. Remarkably, Kapβ2 rapidly dissolved preformed FUS, TAF15, and EWSR1 fibrils within ~15–20 min (Figures 3A–3G and S3A–S3C). By contrast, Kapβ2$^{W460A:W730A}$, Impα and Kapβ1, an anti-FUS-PY-NLS antibody, and HDAC1 had no effect (Figures 3A–3H and S3A–S3C). The half maximal effective concentration (EC$_{50}$) of Kapβ2 was ~2.5 μM (Figure 3G). This disaggregation activity was inhibited by Ran^{GTP}, which disrupts Kapβ2:PY-NLS interactions, but not by Ran^{GDP}, which permits them (Figures 3A, 3C, and 3E). Thus, Kapβ2 rapidly disaggregates PY-NLS bearing cargo, and this activity is likely restricted to the cytoplasm.

To determine the nature of the soluble disaggregated products, we disaggregated His-tagged FUS fibrils with biotinylated-Kapβ2 (bio-Kapβ2). In the presence of buffer or Ran^{GDP}, depletion of bio-Kapβ2 from the soluble disaggregated fraction codepleted the soluble FUS (Figure 3I). Likewise, depletion of His-FUS co-depleted bio-Kapβ2 (Figure 3I). Thus, the major products of Kapβ2-driven disaggregation are soluble Kapβ2:FUS complexes. Ran^{GTP} separated Kapβ2 from disaggregated FUS (Figure 3I). Thus, each Kapβ2 may extract a single FUS monomer from the FUS fibril to form a soluble Kapβ2:FUS complex, which can then be transported to the nucleus. In this way, disaggregated FUS would not reaggregate in the cytoplasm or during transit across the nuclear pore.

The rapidity of Kapβ2-driven disaggregation was unanticipated. Indeed, the protein-disaggregase machinery from yeast, Hsp104, Sse1, Ssa1, and Ydj1 were unable to disaggregate

Figure 2. Kapβ2 Inhibits Seeded Fibrillization of Diverse RBPs with a PY-NLS

(A–F) (A) FUS (5μM) plus or minus FUS fibrils (5% wt/wt), (B) TAF15 (5 μM) plus or minus TAF15 fibrils (5% wt/wt), (C) EWSR1 (5 μM) plus or minus EWSR1 fibrils (5% wt/wt), (D) hnRNPA1 (5 μM) plus or minus hnRNPA1 fibrils (5% wt/wt), (E) hnRNPA2 (5 μM) plus or minus hnRNPA2 fibrils (5% wt/wt), or (F) TDP-43 (5 μM) plus or minus TDP-43 fibrils (5% wt/wt) was incubated with buffer, Kapβ2 (5 μM), Kapβ2$^{W460A:W730A}$ (5 μM), or Impα (5 μM) plus Kapβ1 (5 μM). Fibrillization was assessed by sedimentation. Values are means ± SEM (n = 3).

(G) FUS (5 μM) was incubated with FUS fibrils (5% wt/wt) with or without Kapβ2 (5 μM) and processed for EM. Scale bar, 10 μm.

(H) Disease-linked RBP (5 μM) plus or minus fibrils of the same disease-linked RBP (5% wt/wt) was incubated with buffer, Kapβ2 (5 μM), or Impα (5 μM) plus Kapβ1 (5 μM). Fibrillization was assessed by sedimentation. Values are means ± SEM (n = 3).

See also Figure S2.

FUS, TAF15, and EWSR1 fibrils over this short time frame (Figures S3D–S3F). Even a potentiated Hsp104 variant, Hsp104^{A503S}, required longer times to dissolve FUS and TAF15 fibrils, and was unable to dissolve EWSR1 fibrils (Figures S3D–S3F). Likewise, the human protein-disaggregase system comprised of Hsp110, Hsp70, and Hsp40 (Shorter, 2016) only partially dissolved FUS, TAF15, and EWSR1 fibrils (Figures S3D–S3F). Thus, the ability of Kapβ2 to disaggregate FUS, TAF15, and EWSR1 fibrils was potent compared to canonical disaggregases.

Kapβ2 did not display general protein-disaggregation activity and did not disaggregate proteins without a PY-NLS. Unlike Hsp104, Hsp104^{A503S}, and human Hsp110, Hsp70, and Hsp40, Kapβ2 did not disaggregate denatured luciferase (Figure S3G). Kapβ2 was also unable to disaggregate FUS^{ΔNLS}, TAF15^{ΔNLS}, EWSR1^{ΔNLS} (Figure S3H), or TDP-43 fibrils (Figure 3J).

Remarkably, Impα and Kapβ1 disaggregated TDP-43 and TDP-43^{Q331K} fibrils (Figures 3J and S3I). Impα and Kapβ1 were not as effective as Hsp104^{A503S}, but were more effective than Hsp104 or human Hsp110, Hsp70, and Hsp40 (Figure 3J). Impα plus Kapβ1 had limited activity against TDP-43$^{188-414}$ (that lacks the NLS) fibrils (Figure S3J) or FUS, TAF15, and EWSR1 fibrils (Figures 3A–3F). Collectively, NIRs may function broadly to disaggregate NLS-bearing cargo.

Kapβ2 rapidly disaggregated fibrils formed by disease-linked FUS, EWSR1, and TAF15 variants with an EC$_{50}$ of ~2–3 μM (Figures 3G and 3K). Kapβ2 even partially disaggregated FUS^{P525L} fibrils although the EC$_{50}$ was ~6 μM (Figures 3G and 3K). FUS^{R495X} fibrils were more refractory to Kapβ2 (Figures 3G and 3K). Nonetheless, elevating Kapβ2 levels could dissolve diverse cytoplasmic, disease-associated aggregates formed by RBPs with a PY-NLS.

Figure 3. Kapβ2 Disaggregates Fibrils Formed by Diverse RBPs with a PY-NLS

(A–F) FUS (A and B), TAF15 (C and D), or EWSR1 (E and F) fibrils (5 μM monomer) were incubated with buffer, Kapβ2 (5 μM), Kapβ2$^{W460A:W730A}$ (5 μM), or Impα (5 μM) plus Kapβ1 (5 μM) in the absence or presence of Ran^{GDP} or Ran^{GTP} (25 μM). Disaggregation was assessed by turbidity (A, C, and E). Values are means ± SEM (n = 3). Disaggregation was also assessed by EM (B, D, and F). Scale bar, 0.5 μm.

(G) Kapβ2 EC$_{50}$s for disaggregation of indicated RBP (5 μM monomer) performed as in (A). EC$_{50}$ for FUS^{R495X} could not be determined and is >20 μM.

(H) FUS fibrils (5 μM monomer) were incubated with Kapβ2 (5 μM), HDAC1 (5 or 50 μM), or anti-FUS antibody (5 μM). Disaggregation was assessed by turbidity. Values are means ± SEM (n = 3).

(I) His-FUS fibrils (5 μM monomer) were disassembled with bio-Kapβ2 (5 μM). Soluble disaggregation products were recovered and incubated with Ran^{GDP} or Ran^{GTP} (25 μM). Kapβ2 was depleted with neutravidin Sepharose or His-FUS was depleted with Ni-NTA. Input, bound, and unbound fractions were processed for immunoblot.

(J) TDP-43 fibrils (5 μM monomer) were incubated with Kapβ2 (5 μM), Impα (5 μM) plus Kapβ1 (5 μM), Hsp104 (5 μM) plus Sse1 (1 μM), Ssa1 (1 μM) and Ydj1 (1 μM), or Hsp104^{A503S} (5 μM) plus Sse1 (1 μM), Ssa1 (1 μM) and Ydj1 (1 μM), or Hsp110 (Apg2; 5 μM), Hsp70 (Hsc70; 5 μM), and Hsp40 (Hdj1; 5 μM). Disaggregation was assessed by turbidity. Values are means ± SEM (n = 3).

(legend continued on next page)

Kapβ2 Slowly Disaggregates hnRNPA1 and hnRNPA2 Fibrils

Kapβ2 slowly dissolved WT and disease-linked hnRNPA1 and hnRNPA2 fibrils, whereas Kapβ2[W460A:W730A] did not (Figures 3L and 3M). Kapβ2 was not as effective as Hsp104[A503S], but was more effective than Hsp104 or human Hsp110, Hsp70, and Hsp40 (Figures 3L and 3M). hnRNPA1[D262V], hnRNPA1[D262N], and hnRNPA2[D290V] fibrils were more difficult clients for disaggregation by Kapβ2 (Figures 3L and 3M). hnRNPA1[Δ263-289] or hnRNPA2[Δ293-319] fibrils, which lack the PY-NLS, could not be disassembled by Kapβ2 (Figures 3L and 3M). Thus, Kapβ2 engages the PY-NLS to slowly disassemble WT and disease-linked hnRNPA1 and hnRNPA2 fibrils.

Kapβ2 Rapidly Disperses Liquid Drops Formed by FUS and hnRNPA1

FUS and hnRNPA1 can undergo LLPS to form macroscopic liquid droplets (Molliex et al., 2015; Patel et al., 2015). However, these droplets are not required for fibrillization of FUS, hnRNPA1, or other RBPs with PrLDs, which fibrillize under conditions where liquid droplets do not (Lin et al., 2015). Indeed, under our conditions employed above, RBPs rapidly fibrillize and do not dwell in macroscopic liquid states (Couthouis et al., 2011, 2012; Johnson et al., 2009; Kim et al., 2013; Sun et al., 2011).

To assess how Kapβ2 affects FUS LLPS, we omitted TEV protease and increased FUS concentration, which enables condensation of spherical FUS drops that readily fuse indicating liquid behavior (Figure S4A; Movie S1). Kapβ2 abolished FUS LLPS, whereas Kapβ2[W460A:W730A] had no effect (Figure S4A). Thus, Kapβ2 engages the FUS PY-NLS to prevent LLPS.

Next, we assessed FUS[P525L], which formed smaller and more irregular droplet structures (Figure S4B). Thus, the P525L mutation impairs formation of large FUS liquid droplets and promotes assembly of smaller aberrant, more solid-like structures (Figure S4B) (Murakami et al., 2015). Kapβ2 abolished formation of these FUS[P525L] assemblies, whereas Kapβ2[W460A:W730A] had little effect (Figure S4B). Thus, Kapβ2 antagonizes FUS[P525L] phase separation.

Kapβ2, but not Kapβ2[W460A:W730A], rapidly dissolved preformed FUS liquids in seconds (Figure S4C; Movies S1 and S2). Thus, Kapβ2 engages the FUS PY-NLS to rapidly reverse FUS LLPS. Kapβ2 also rapidly dissolved preformed FUS[P525L] structures, whereas Kapβ2[W460A:W730A] was less effective (Figure S4D; Movies S3 and S4).

Could Kapβ2 dissolve phase-separated hnRNPA1 liquids? At 4°C, hnRNPA1 rapidly condenses into a viscous liquid phase (Figure S4E), which was readily pipetted and rapidly resolved at 25°C (Molliex et al., 2015). Rheology confirmed that this phase was a viscous liquid as the storage modulus (G′) of ~40 Pa was smaller than the loss modulus (G″) of ~105 Pa (Figures S4F and S4G). Kapβ2 dissolved viscous hnRNPA1 liquids at 4°C, whereas Kapβ2[W460A:W730A] was ineffective and only mildly reduced G′ and G″ indicating decreased viscoelasticity (Figures S4E–S4G). Thus, Kapβ2 engages the hnRNPA1 PY-NLS to reverse hnRNPA1 LLPS.

Kapβ2 Dissolves Aberrant FUS and hnRNPA1 Hydrogels

Fibrils formed by the PrLDs or full-length FUS, TAF15, EWSR1, hnRNPA1, and hnRNPA2 can associate into macroscopic hydrogels (Harrison and Shorter, 2017). These stable assemblies may originate from functional liquid states of RNP granules and are closely tied to neurotoxicity (Molliex et al., 2015; Murakami et al., 2015; Patel et al., 2015). Could Kapβ2 reverse aberrant phase transitions to these structures? At 4°C, FUS formed hydrogels comprised of fibrillar networks (Figures 4A and 4B), which could not be pipetted or disassembled by shifting to 25°C. FUS formed strong gels with G′ at ~4,235 Pa (Figure 4C) and G″ at ~866 Pa (Figure 4D). These measures of elasticity (G′) and viscosity (G″) indicate that FUS hydrogels have similar material properties to an ~0.5%–1% agarose gel and are stiffer than cells and some human tissues (Levental et al., 2007). Remarkably, Kapβ2 dissolved these stable FUS hydrogels by dismantling the fibrillar matrix underlying the gel (Figures 4B and 4G). After dissolution by Kapβ2, G′ and G″ were ~0.12 Pa, consistent with obliteration of FUS fibrils (Figures 4C and 4D). Kapβ2[W460A:W730A] had no visible effect (Figure 4G), but reduced G′ and G″ by ~30%, indicating decreased viscoelasticity (Figures 4E and 4F). Thus, FUS hydrogels are not irreversible, but can be rapidly deconstructed by Kapβ2. Kapβ2 could not dissolve hydrogels formed by a FUS PrLD fragment, FUS[1–214] (Figure 4H). Thus, Kapβ2 engages the FUS PY-NLS to dissolve FUS hydrogels.

Could Kapβ2 disrupt hnRNPA1 hydrogels? At 4°C, hnRNPA1 forms solid-like gels very slowly after rapidly populating a reversible viscous liquid phase at early times (Figure S4E) (Molliex et al., 2015). After a few weeks, hnRNPA1 liquids mature into solid, strong gels comprised of fibril networks, which cannot be pipetted (Figures 4I and 4J). The G′ of hnRNPA1 gels was ~21,099 Pa and G″ was ~7,438 Pa (Figures 4K and 4L), which are material properties akin to an ~1%–1.5% agarose gel (Levental et al., 2007). Kapβ2 partially disassembled hnRNPA1 hydrogels and disrupted the underlying fibril network (Figures 4J and 4M). However, some parts of the gel remained intact (Figure 4M). The residual hnRNPA1 gel was greatly weakened by ~99% (Figures 4K and 4L). Kapβ2[W460A:W730A] did not dissolve hnRNPA1 hydrogels but weakened them by ~40%–50% (Figures 4K and 4L). This effect was specific as GFP did not alter G′ and G″ (Figures 4N and 4O). Kapβ2[W460A:W730A] may weaken hnRNPA1 hydrogels
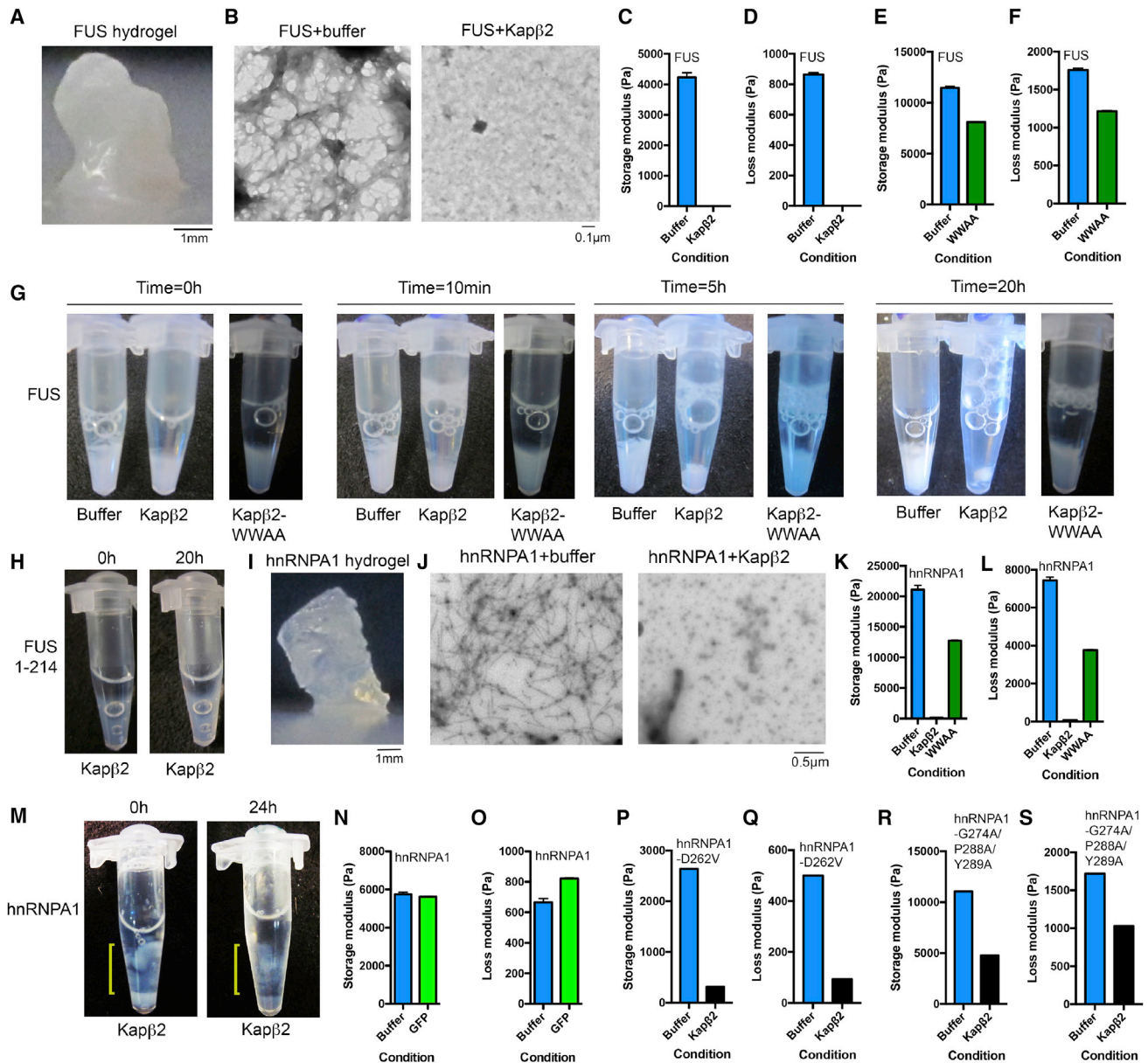

(K) RBP fibrils (5 μM monomer) were incubated with buffer or Kapβ2 (5 μM). Disaggregation was assessed by turbidity. Values are means ± SEM (n = 3).

(L) hnRNPA1, hnRNPA1[D262V], hnRNPA1[D262N], or hnRNPA1[ΔNLS] fibrils (5 μM monomer) were incubated with Kapβ2 (5 μM), Kapβ2[W460A:W730A] (5 μM), Hsp104 (5 μM) plus Sse1 (1 μM), Ssa1 (1 μM) and Ydj1 (1 μM), Hsp104[A503S] (5 μM) plus Sse1 (1 μM), Ssa1 (1 μM) and Ydj1 (1 μM), or Hsp110 (Apg2; 5 μM), Hsp70 (Hsc70; 5 μM), and Hsp40 (Hdj1; 5 μM). Disaggregation was assessed by sedimentation. Values are means ± SEM (n = 3).

(M) hnRNPA2, hnRNPA2[D290V], or hnRNPA2[ΔNLS] fibrils (5 μM monomer) were incubated with Kapβ2 (5 μM), Kapβ2[W460A:W730A] (5 μM), Hsp104 (5 μM) plus Sse1 (1 μM), Ssa1 (1 μM) and Ydj1 (1 μM), Hsp104[A503S] (5 μM) plus Sse1 (1 μM), Ssa1 (1 μM) and Ydj1 (1 μM), or Hsp110 (Apg2; 5 μM), Hsp70 (Hsc70; 5 μM), and Hsp40 (Hdj1; 5 μM). Disaggregation was assessed by sedimentation. Values are means ± SEM (n = 3).

See also Figure S3.

Figure 4. Kapβ2 Dissolves FUS and hnRNPA1 Hydrogels

(A) Macroscopic hydrogel formed by FUS (240 μM). Scale bar, 1 mm.

(B) EM of FUS hydrogel treated with buffer reveals a fibrillar network that is disrupted by Kapβ2. Molar ratio of Kapβ2:FUS = 0.675. Scale bar, 0.1 μm.

(C and D) Storage modulus (C) and loss modulus (D) of FUS hydrogels treated with buffer or Kapβ2. Molar ratio of Kapβ2:FUS = 0.675. Values are means ± SEM.

(E and F) Storage modulus (E) and loss modulus (F) of FUS hydrogels treated with buffer or Kapβ2$^{W460A:W730A}$. Molar ratio of Kapβ2$^{W460A:W730A}$:FUS = 0.415. Values are means ± SEM.

(G) FUS hydrogels were treated with buffer, Kapβ2, or Kapβ2$^{W460A:W730A}$. Molar ratio of Kapβ2/Kapβ2$^{W460A:W730A}$:FUS = 0.563.

(H) FUS$^{1–214}$ hydrogels were treated with Kapβ2. Molar ratio of Kapβ2:FUS$^{1–214}$ = 0.15.

(I) Macroscopic hydrogel formed by hnRNPA1 (3.1 mM). Scale bar, 1 mm.

(J) EM of solid-like hnRNPA1 gels treated with buffer reveals fibrillar network (left) that is disrupted by Kapβ2 (right). Molar ratio of Kapβ2:hnRNPA1 = 0.13. Scale bar, 0.5 μm.

(K and L) Storage modulus (K) and loss modulus (L) of hnRNPA1 gels treated with buffer, Kapβ2, or Kapβ2$^{W460A:W730A}$. Molar ratio of Kapβ2:hnRNPA1 = 0.13. Values are means ± SEM.

(M) Solid-like hnRNPA1 gels were treated with Kapβ2. Note partial disassembly of hnRNPA1 hydrogel by Kapβ2 over time (indicated by the bracket). Molar ratio of Kapβ2:hnRNPA1 = 0.13.

(N and O) Storage modulus (N) and loss modulus (O) of hnRNPA1 gels treated with buffer or GFP. Molar ratio of GFP:hnRNPA1 = 0.27. Values are means ± SEM.

by breaking intermolecular contacts, an activity that enables Kapβ2 to traverse the nuclear pore (Schmidt and Görlich, 2016). Thus, an ability to break intermolecular contacts and bind the cargo PY-NLS enables Kapβ2 to dismantle strong gels formed by RBPs with a PY-NLS.

hnRNPA1^{D262V} rapidly formed hydrogels overnight and at lower concentrations than hnRNPA1. Indeed, hnRNPA1^{D262V} only briefly populated a liquid phase (Molliex et al., 2015). Kapβ2 was unable to visibly dissolve hnRNPA1^{D262V} hydrogels. Nonetheless, even with hnRNPA1^{D262V} in excess, Kapβ2 severely weakened the hydrogel as G′ and G″ declined by ~82%–88% (Figures 4P and 4Q). Indeed, Kapβ2 converted strong hnRNPA1^{D262V} gels that could not be pipetted to weak gels that were readily pipetted. Thus, MSP-linked hnRNPA1^{D262V} forms hydrogels that are stronger and more difficult to reverse, which may underlie MSP pathogenesis. Nonetheless, Kapβ2 liquidizes solid-like hnRNPA1^{D262V} gels and thus reverses aberrant phase transitions.

Kapβ2 was unable to dissolve hydrogels formed by hnRNPA1$^{G274A:P288A:Y289A}$, which bears PY-NLS mutations that reduce Kapβ2 binding (Lee et al., 2006). Nonetheless, Kapβ2 weakened this structure by ~57% (Figures 4R and 4S). Thus, Kapβ2 weakens hydrogels formed by RBPs that lack a PY-NLS, but weakens, liquidizes, and dissolves hydrogels formed by RBPs with a PY-NLS.

Kapβ2 Antagonizes Cytoplasmic Aggregation and Restores Nuclear Localization of FUS, EWSR1, hnRNPA1, and hnRNPA2

Could Kapβ2 antagonize RBP aggregation *in vivo*? First, we turned to yeast models where FUS, EWSR1, hnRNPA1, and hnRNPA2 mislocalize to the cytoplasm and aggregate as in neurodegenerative disease (Couthouis et al., 2011). Kapβ2, but not Kapβ2$^{W460A:W730A}$, prevented formation of cytoplasmic FUS, EWSR1, hnRNPA1, and hnRNPA2 foci, and localized these RBPs to the nucleus (Figures 5A and 5B). Kapβ2 conferred this effect without reducing FUS, hnRNPA1, or hnRNPA2 expression, whereas EWSR1 expression was reduced (Figure S5A). Kapβ2 chaperone activity extended to disease-linked FUS^{R521C}, FUS^{R521H}, hnRNPA1^{D262V}, hnRNPA1^{D262N}, and hnRNPA2^{D290V} (Figures 5A and 5B). By contrast, Kapβ2 did not prevent cytoplasmic aggregation of FUS^{P525L} and FUS^{R495X} (Figures 5A and 5B). Thus, in cells, Kapβ2 chaperone activity depends on cargo possessing an intact PY-NLS.

To assess Kapβ2 disaggregation activity in yeast, we expressed GFP-FUS from an inducible copper promoter for 2 hr to allow cytoplasmic FUS aggregates to accumulate (Figure 5C). Indeed, at this time, all cells had cytoplasmic FUS foci and FUS was not in the nucleus (Figures 5C and 5D). FUS expression was then turned off and Kapβ2 or Kapβ2$^{W460A:W730A}$ was expressed for 3 hr (Figure 5C). Immunoblots confirmed that FUS levels declined and Kapβ2 or Kapβ2$^{W460A:W730A}$ was expressed as ex-

pected (Figure S5B). Kapβ2, but not Kapβ2$^{W460A:W730A}$, eliminated preformed GFP-FUS foci and localized GFP-FUS to the nucleus (Figures 5C and 5D). Similar results were obtained if FUS expression was not turned off (Figure 5D). Thus, Kapβ2 reverses cytoplasmic FUS aggregation and restores FUS to the nucleus.

Kapβ2 Reduces FUS Accumulation in SGs

Many RBPs with PrLDs become concentrated in SGs, which are cytoplasmic RNP granules that form upon stress. Elevated local concentrations of RBPs with PrLDs in SGs accentuates the risk of aberrant phase transitions and pathological fibrillization. Thus, restricting accumulation of RBPs with PrLDs in SGs could be neuroprotective (March et al., 2016). In stressed human cells, Kapβ2 is recruited to SGs (Figure S5C). Elevating Kapβ2 expression did not inhibit SG formation as the SG assembly factor, G3BP1, still formed SGs (Figures 5E and S5D). However, increased Kapβ2 expression inhibited FUS accumulation in SGs, whereas Kapβ2$^{W460A:W730A}$ did not (Figures 5E and 5F). Deletion of the FUS PY-NLS prevented Kapβ2 from inhibiting FUS accumulation in SGs (Figures 5G and S5D). Kapβ2, but not Kapβ2$^{W460A:W730A}$, reduced accumulation of ALS-linked FUS^{R518K}, FUS^{R521C}, and FUS^{R521H} in SGs (Figures 5G and S5D). Thus, Kapβ2 prevents FUS accumulation in SGs but not SG biogenesis.

Did Kapβ2 prevent FUS accumulation in SGs indirectly by increasing FUS nuclear import? To answer this question, we used a Kapβ2 mutant, Kapβ2^{TL}, which harbors a truncated H8 loop. Kapβ2^{TL} engages PY-NLS-bearing cargo with high affinity, but the truncated H8 loop prevents Ran^{GTP} from releasing bound cargo thus disabling nuclear import (Chook et al., 2002). Like Kapβ2, Kapβ2^{TL} prevented and reversed FUS fibrillization (Figures S5E and S5F). Thus, Kapβ2^{TL} chaperones and disaggregates FUS, but is defective in nuclear import (Chook et al., 2002). Like Kapβ2, Kapβ2^{TL} prevented FUS accumulation in SGs (Figures 5E and 5F). Thus, Kapβ2 prevents FUS accumulation in SGs directly and not indirectly via increased nuclear import of FUS.
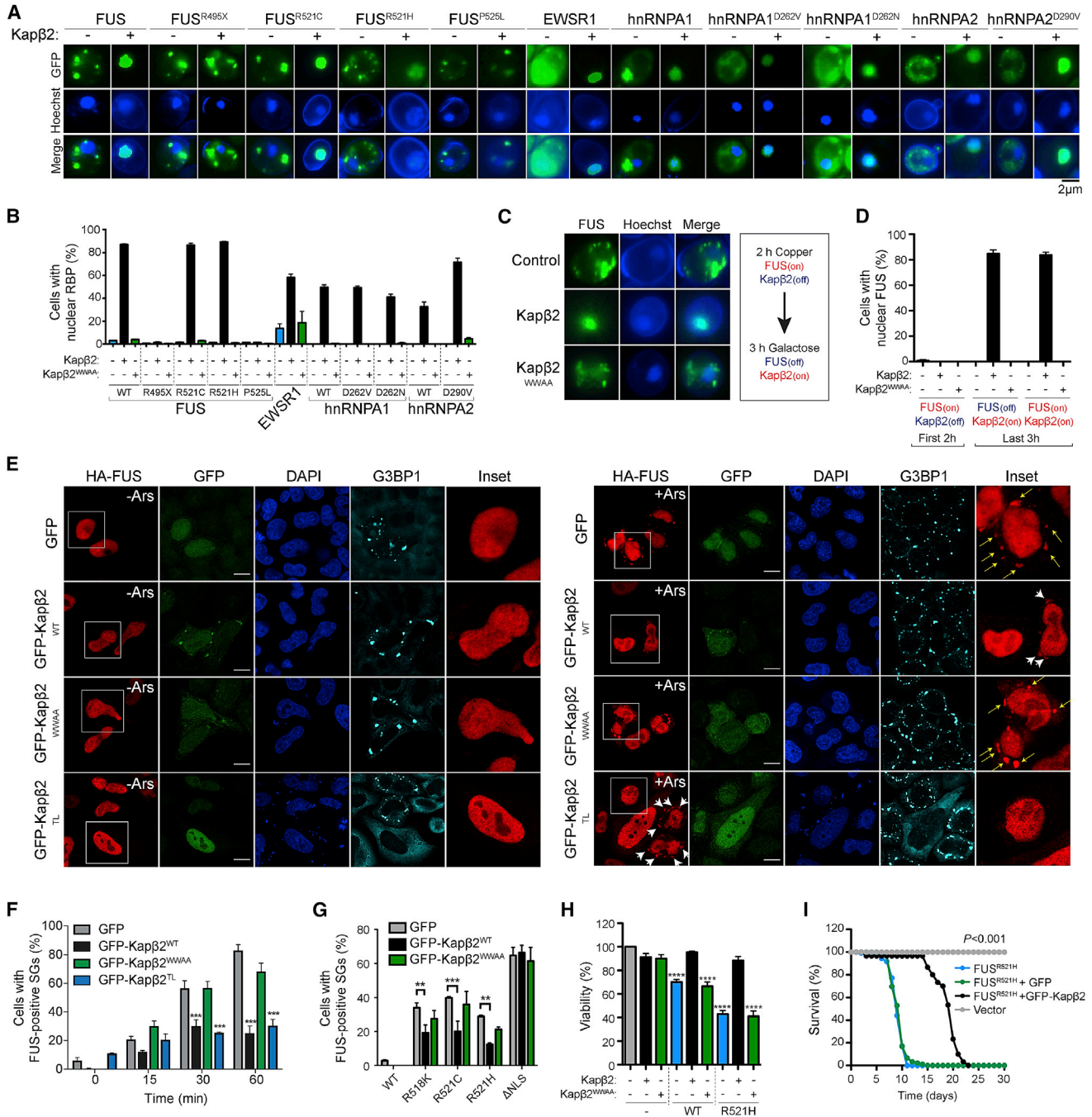
Could Kapβ2 reverse FUS accumulation in SGs in human cells? To answer this question, we expressed ALS-linked FUS^{R521C} for 24 hr, by which time ~12% of cells have FUS^{R521C} in SGs (Figure S5G). We then expressed Kapβ2 or Kapβ2^{TL} for 24 hr, after which only ~5.3% of cells had FUS^{R521C} in SGs, whereas GFP or Kapβ2$^{W460A:W730A}$ had no effect (Figure S5G). Thus, Kapβ2 and Kapβ2^{TL} can selectively extract FUS^{R521C} from SGs.

Next, we used human neural progenitor cells edited with CRISPR/Cas9 to express endogenous levels of FUS or ALS-linked FUS^{R521H}. Here, Kapβ2 reduced accumulation of FUS- and FUS^{R521H}-positive SGs, whereas Kapβ2$^{W460A:W730A}$ was less effective (Figures S6A and S6B). Thus, Kapβ2 antagonizes accumulation of FUS and FUS^{R521H} in SGs in diverse cell types.

(P and Q) Storage modulus (P) and loss modulus (Q) of hnRNPA1^{D262V} gels treated with buffer or Kapβ2. Molar ratio of Kapβ2:hnRNPA1^{D262V} = 0.76. Values are means ± SEM.

(R and S) Storage modulus (R) and loss modulus (S) of hnRNPA1$^{G274A:P288A:Y289A}$ gels treated with buffer or Kapβ2. Molar ratio of Kapβ2:hnRNPA1$^{G274A:P288A:Y289A}$ = 0.13. Values are means ± SEM.

See also Figure S4 and Movies S1, S2, S3, and S4.

Figure 5. Kapβ2 Antagonizes RBP Phase Transitions and Toxicity *In Vivo*

(A and B) Fluorescence microscopy of yeast expressing indicated GFP-tagged RBP and Kapβ2 or vector control. Hoechst staining marks nuclei (blue). Scale bar, 2 μm (A). The percentage of cells with RBP in the nucleus and lacking cytoplasmic RBP foci is shown (B). Values are means ± SEM (n = 3).

(C) Fluorescence microscopy of yeast expressing GFP-FUS from the copper promoter for 2 hr (upper panel) that were shifted to galactose media without copper for 3 hr to induce Kapβ2 or Kapβ2$^{W460A:W730A}$ and switch off FUS (lower two panels). Hoechst staining marks nuclei (blue).

(D) Quantification of (C) and an additional condition where GFP-FUS was expressed from the copper promoter for the first 2 hr and then Kapβ2 or Kapβ2$^{W460A:W730A}$ expression was induced for 3 hr without switching off FUS. The percentage of cells with FUS in the nucleus and lacking cytoplasmic FUS foci is shown. Values are means ± SEM (n = 3).

(E) HeLa cells were transfected with HA-FUS plus GFP, GFP-Kapβ2, GFP-Kapβ2$^{W460A:W730A}$, or GFP-Kapβ2^{TL}. Cells were treated with 0.5 mM sodium arsenite for 60 min, and immunostained with anti-HA, anti-G3BP1, and DAPI. Yellow arrows denote FUS-positive SGs. Cells at pre- (−Ars) and 60 min post-arsenite treatment (+Ars) are shown. White arrowheads denote FUS-positive SGs in cells that do not express GFP-Kapβ2^{WT} or GFP-Kapβ2^{TL}. Scale bar, 10 μm.

(legend continued on next page)

Kapβ2 Buffers FUS Toxicity

Expression of FUS or ALS-linked FUS[R521H] in human HEK293T cells causes toxicity (Sun et al., 2011). This toxicity was reduced by Kapβ2 but not Kapβ2[W460A:W730A] (Figures 5H and S6C). Thus, elevating Kapβ2 expression in human cells mitigates FUS and FUS[R521H] toxicity.

Kapβ2 Restores Expression of FUS mRNA Targets in ALS-Patient Fibroblasts

Ideally, Kapβ2 would restore any loss of FUS function by returning FUS to the nucleus where FUS regulates pre-mRNA splicing and gene expression (Harrison and Shorter, 2017). Thus, we increased Kapβ2 expression in fibroblasts from three control individuals with WT FUS and three ALS patients with FUS[R521H] (Figure S6D). In FUS[R521H] ALS-patient fibroblasts, expression of three FUS mRNA targets, TPST2, WNT5A, and ITGA3, was decreased ~2-fold compared to controls (Figure S6E). In FUS[R521H] ALS-patient fibroblasts, Kapβ2 restored TPST2, WNT5A, and ITGA3 expression back to control levels (Figure S6E). Thus, increasing Kapβ2 expression could combat FUS loss of function in ALS/FTD.

Reducing Kapβ2 Enhances FUS-Linked Neurodegeneration in *Drosophila*

Does reducing Kapβ2 levels enhance FUS-linked neurodegeneration *in vivo*? To answer this question, we used *Drosophila* where expression of ALS-linked FUS variants recapitulates several ALS phenotypes, including locomotion defects, neurodegeneration, cytoplasmic FUS mislocalization and aggregation, and reduced lifespan (Daigle et al., 2013). We expressed FUS, FUS[R521H], FUS[P525L], or FUS[R518K] in the fly eye, which causes a rough eye phenotype and neurodegeneration (Figure S7A). FUS induces a slight rough eye phenotype, whereas FUS[R521H], FUS[P525L], and FUS[R518K] are more severe (Figures S7A and S7B). We reduced Kapβ2 expression by ~60%–80% using RNAi in two independent lines (Figure S7C), which enhanced degeneration caused by FUS, FUS[R521H] and FUS[R518K], but not FUS[P525L] (Figures S7A and S7B). Thus, Kapβ2 mitigates FUS, FUS[R521H], and FUS[R518K] toxicity in the animal nervous system.

Elevating Kapβ2 Rescues FUS-Linked Neurodegeneration and Lifespan in *Drosophila*

We next tested whether elevated Kapβ2 concentrations mitigated FUS[R521H]-mediated motor neuron degeneration in fly (Daigle et al., 2013). Expression of FUS[R521H] in adult motor neurons reduced mean fly lifespan from ~48.6 days to ~9.2 days (Figure 5I). Co-expression of Kapβ2 in adult motor neurons increased lifespan to ~18.6 days, whereas co-expression of GFP had no effect (Figure 5I). Thus, Kapβ2 mitigates FUS[R521H] motor-neuron toxicity *in vivo*.

Kapβ2 Prevents hnRNPA1 and hnRNPA2 Accumulation in SGs

We extended our studies to hnRNPA1 and hnRNPA2 in human cells. Increased expression of Kapβ2 but not Kapβ2[W460A:W730A] reduced SG-associated hnRNPA1 (Figures 6A and 6B) and hnRNPA2 (Figures 6C and 6D) without affecting SG biogenesis. Thus, Kapβ2 also restricts hnRNPA1 and hnRNPA2 accumulation in SGs.

Kapβ2 Rescues hnRNPA2-Linked Muscle Degeneration in *Drosophila*

Finally, we tested whether Kapβ2 protects against hnRNPA2[D290V]-mediated degeneration in a MSP-relevant tissue, i.e., muscle, in an intact animal. MSP-hnRNPA2[D290V] most commonly presents with inclusion body myopathy (Kim et al., 2013). Hence, we tested whether Kapβ2 mitigates muscle degeneration caused by MSP-linked hnRNPA2[D290V] in fly.

When expressed in fly indirect flight muscles, hnRNPA2 caused mild disruption of muscle fiber organization and partial wasting revealed by staining F-actin with Texas Red-phalloidin (Figure 7A, white arrows). hnRNPA2 was mostly nuclear and detergent soluble (Figures 7B and 7C). By contrast, MSP-linked hnRNPA2[D290V] caused severe muscle degeneration with disorganization and loss of muscle fibers (Figure 7A, white arrows). hnRNPA2[D290V] exhibited extensive cytoplasmic mislocalization and aggregation (Figure 7B, white arrows), nuclear exclusion (Figure 7B, yellow arrowheads), and detergent insolubility (Figure 7C). Kapβ2 reduced disruption of muscle fibers and partial wasting caused by hnRNPA2 and prevented hnRNPA2[D290V]-driven muscle degeneration (Figure 7A). Indeed, flies now had normal muscles comparable to non-transgenic controls (Figure 7A).

Kapβ2 reduced the amount of hnRNPA2 and hnRNPA2[D290V] in detergent-insoluble (i.e., urea soluble) fractions by ~6-fold and ~2.2-fold, respectively (Figure 7C). Kapβ2 mildly reduced hnRNPA2 and hnRNPA2[D290V] expression (Figure 7D). This effect of Kapβ2 on hnRNPA2 and hnRNPA2[D290V] expression is specific as RNAi of fly Kapβ2 increased hnRNPA2 and hnRNPA2[D290V] (Figure S7D). This increase in hnRNPA2[D290V] is accompanied by a ~1.4-fold increase of hnRNPA2[D290V] in the detergent-insoluble fraction (Figure S7E). Thus, Kapβ2 inhibits hnRNPA[D290V] aggregation. Indeed, Kapβ2 reduced cytoplasmic hnRNPA2[D290V] aggregation, restored hnRNPA2[D290V] to the nucleus, and
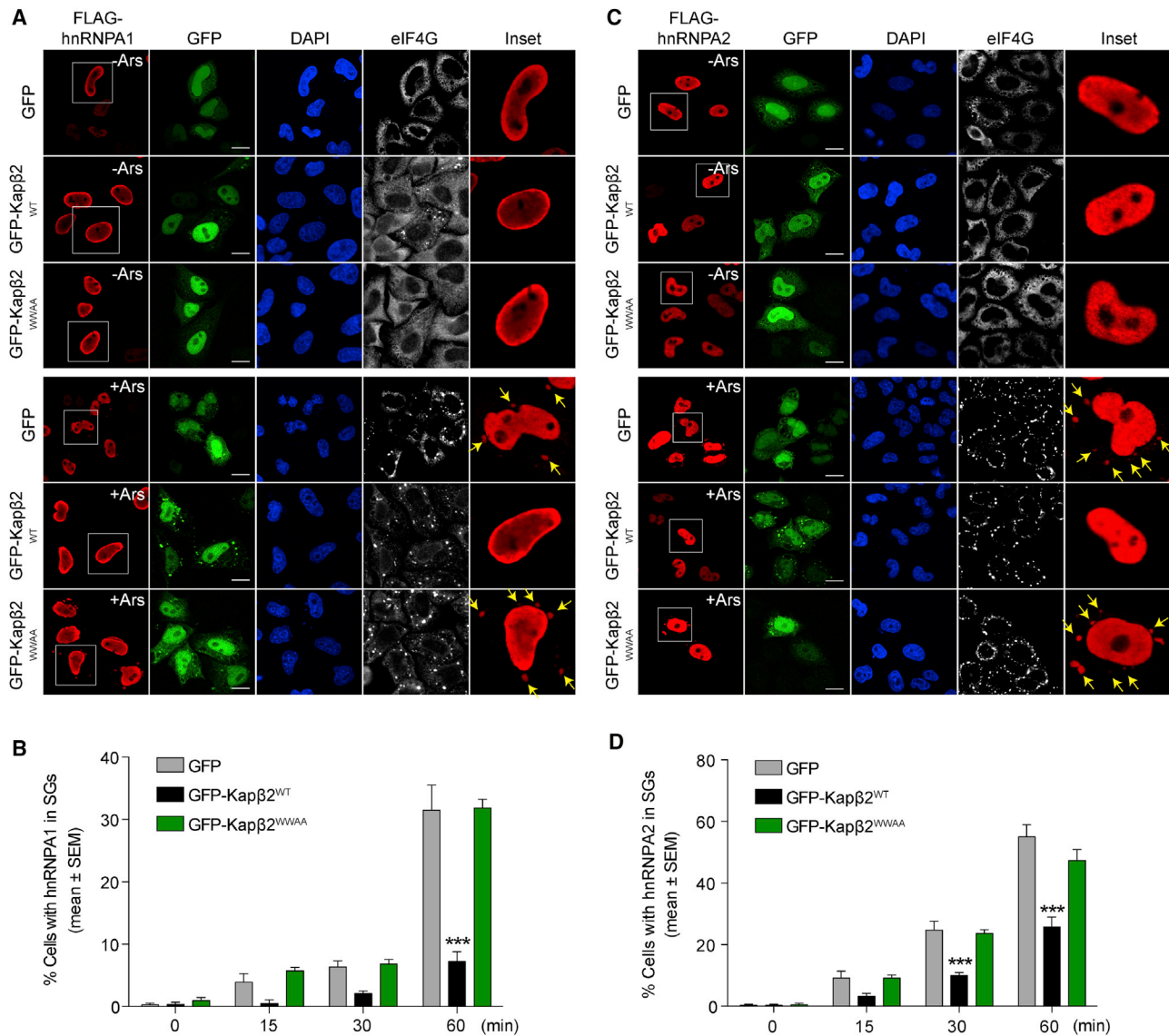
(F) Quantification of (E). The percentage of transfected cells with FUS-positive SGs is shown. ***p < 0.001 two-way ANOVA, Bonferroni's multiple comparisons test. Values are means ± SEM (n = 3–4).

(G) HeLa cells were transfected with GFP or GFP-Kapβ2 together with HA-FUS[R518K], HA-FUS[R521C], HA-FUS[R521H], or HA-FUS[ΔNLS]. Cells were fixed and immunostained as in (E). The percentage of transfected cells with FUS-positive SGs is shown. **p < 0.01, ***p < 0.001 by two-way ANOVA, Bonferroni's multiple comparisons test. Values are means ± SEM (n = 6).

(H) Kapβ2 but not Kapβ2[W460A:W730A] suppressed FUS and FUS[R521H] toxicity in HEK293T cells. Cell viability was assessed by MTT assay. Values are means ± SEM (n = 7). One-way ANOVA with post hoc Dunnett's multiple comparisons test was used to compare the control (gray) to other conditions (**** denotes p ≤ 0.0001).

(I) Kapβ2 but not GFP mitigates shortened lifespan of flies expressing FUS[R521H] in motor neurons. A log rank test for trend was used to test for differences between survival curves and a log rank Mantel Cox test for pairwise comparisons between FUS[R521H] versus FUS[R521H] plus Kapβ2 and FUS[R521H] plus GFP versus FUS[R521H] plus Kapβ2. All revealed significant differences with p < 0.001.

See also Figures S5, S6, and S7.

Figure 6. Kapβ2 Reduces hnRNPA1 and hnRNPA2 Accumulation in SGs

(A) HeLa cells were transfected with GFP or GFP-Kapβ2 together with Flag-hnRNPA1. Cells were treated with 0.5 mM sodium arsenite, and immunostained with anti-Flag, anti-eIF4G, and DAPI. Arrows indicate hnRNPA1-positive SGs. Cells at pre- (−Ars) and 60 min post-arsenite treatment (+Ars) are shown. Scale bar, 10 μm.

(B) Quantification of (A). The percentage of transfected cells with hnRNPA1-positive SGs is shown. ***p < 0.001 by two-way ANOVA, Bonferroni's multiple comparisons test. Values are means ± SEM (n = 3).

(C) HeLa cells were transfected with GFP or GFP-Kapβ2 together with Flag-hnRNPA2. Cells were treated with 0.5 mM sodium arsenite and immunostained with anti-Flag, anti-eIF4G, and DAPI. Arrows indicate hnRNPA2-positive SGs.
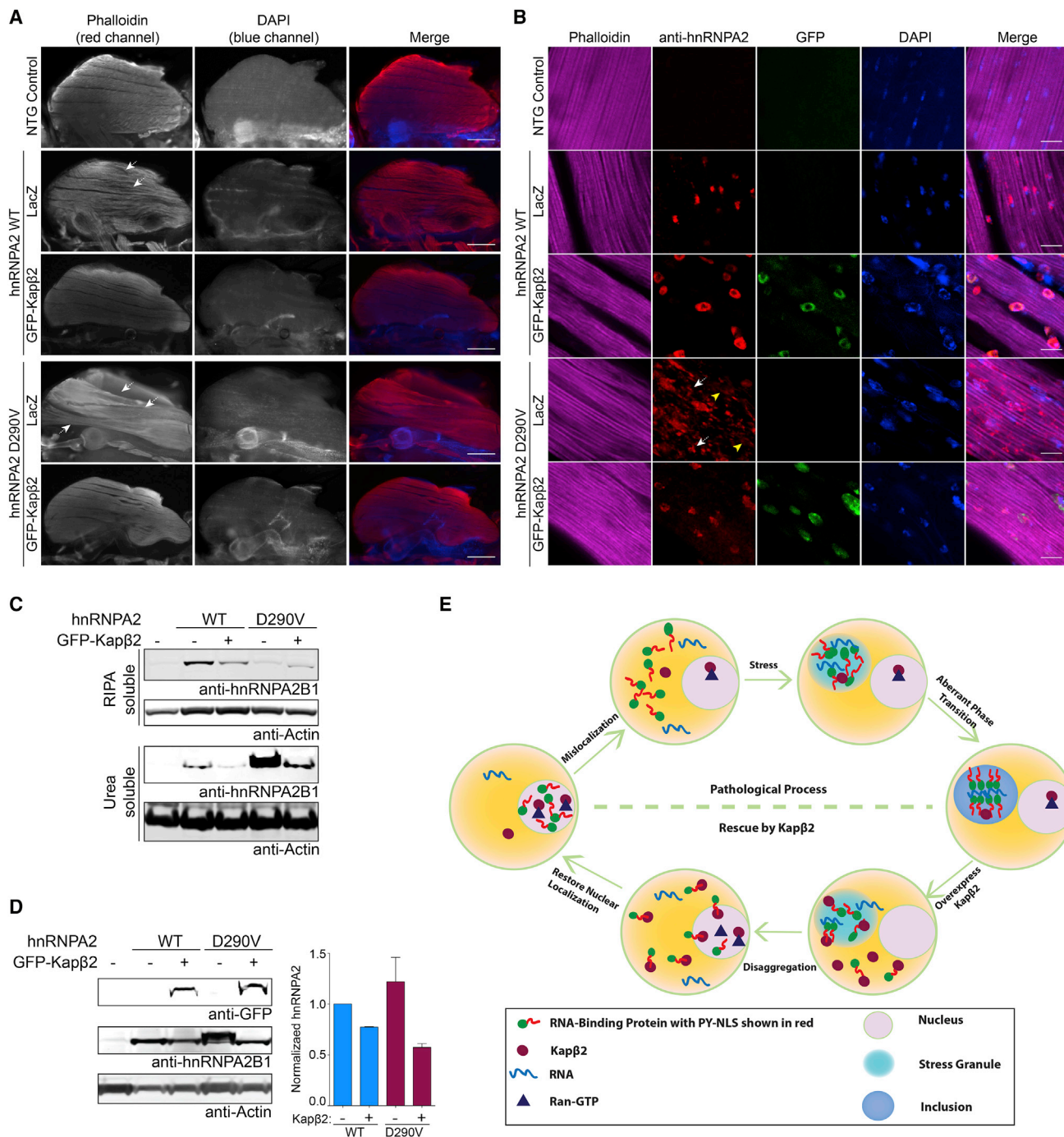
(D) Quantification of (C). The percentage of transfected cells with hnRNPA1-positive SGs is shown. ***p < 0.001 by two-way ANOVA, Bonferroni's multiple comparisons test. Values are means ± SEM (n = 3).

reduced hnRNPA2[D290V]-induced muscle degeneration (Figures 7A and 7B). Thus, Kapβ2 could have therapeutic utility in MSP.

DISCUSSION

Here, we establish that NIRs *reverse* deleterious fibrillization and aberrant phase transitions of disease-linked RBPs with PrLDs by engaging their NLSs (Figure 7E). Thus, NIRs do not merely func-

tion in nuclear import and are not merely chaperones (Jäkel et al., 2002; Milles et al., 2013). Rather, they perform additional functions in reversing aberrant phase transitions and disaggregating their cargo in the cytoplasm. We establish that NIRs also selectively extract their cargos from condensed liquid phases thereby regulating functional phase separation. Collectively, these activities enable NIRs to shape the contents and architecture of cytoplasmic membraneless organelles. Thus, NIRs profoundly

Figure 7. Kapβ2 Reduces hnRNPA2^{D290V} Aggregation and Toxicity *In Vivo*

(A) Adult flies were dissected to expose the dorsal longitudinal indirect flight muscle and stained with Texas red-phalloidin (red) to label F-actin in muscle fibers and DAPI (blue) to mark nuclei. Flies expressing hnRNPA2 under control of the MHC-Gal4 driver showed mild degeneration indicated by partial wasting of muscle fibers (white arrows). hnRNPA2^{D290V} caused severe muscle degeneration indicated by shrinking and loss of muscle fibers (white arrows). Muscle degeneration was rescued by Kapβ2 and resulted in muscles that were similar to non-transgenic (NTG) controls. Scale bar, 0.2 mm.

(B) hnRNPA2 localizes to nuclei, whereas hnRNPA2^{D290V} accumulates in cytoplasmic inclusions (white arrows). hnRNPA2^{D290V} is excluded from the nucleus (yellow arrowhead). Kapβ2 reduces cytoplasmic aggregation and restores hnRNPA2^{D290V} to the nucleus. Scale bar, 20 μm.

(C) Thoraces of adult flies were dissected and sequentially extracted to examine hnRNPA2 solubility. Actin serves as a loading control.

(D) Thoraces of adult flies were processed for immunoblot with antibodies against GFP and hnRNPA2. Actin serves as a loading control. Quantification of hnRNPA2 levels is shown. Values are means ± SD (n = 2).

(legend continued on next page)

influence cellular organization beyond their canonical role in nuclear import.

Impα and Kapβ1 engage the cNLS to prevent and reverse TDP-43 fibrillization, whereas Kapβ2 engages PY-NLSs to prevent and reverse FUS, TAF15, EWSR1, hnRNPA1, and hnRNPA2 fibrillization. Kapβ2 prevents and reverses FUS LLPS (Hofweber et al., 2018; Yoshizawa et al., 2018; in this issue of Cell). Kapβ2 also reverses aberrant phase transitions of FUS and hnRNPA1 that result in fibrillar hydrogels, which are linked to neurodegeneration (Molliex et al., 2015; Murakami et al., 2015; Patel et al., 2015). This potent disaggregation activity of NIRs extends to disease-linked RBP variants such as TDP-43^{Q331K}, FUS^{R521H}, hnRNPA1^{D262V}, and hnRNPA2^{D290V}. Even FUS^{P525L}, which binds Kapβ2 with reduced affinity (Zhang and Chook, 2012), could be chaperoned and disaggregated by high concentrations of Kapβ2. Nonetheless, deletion of the NLS from RBPs reduced NIR chaperone or disaggregation activity. Thus, the NLS is not simply a signal that promotes nuclear import. Rather, the NLS is an anti-aggregation and disaggregation signal, which ensures nuclear cargo is chaperoned and disaggregated in the cytoplasm. Notably, ~75% of human PrLD-containing proteins harbor a cNLS or PY-NLS. Thus, NIRs likely function broadly to antagonize aberrant phase transitions of proteins with PrLDs.

A major therapeutic goal in ALS/FTD is to restore nuclear function of RBPs such as FUS that are mislocalized to cytoplasmic aggregates in degenerating neurons. FUS fibril dissolution by Kapβ2 yields soluble Kapβ2:FUS complexes, which are competent for nuclear transport. Upon arrival in the nucleus, Ran^{GTP} completes the disaggregation reaction by releasing FUS from Kapβ2. FUS can then perform its nuclear function and Kapβ2 can be recycled to catalyze further rounds of chaperone, disaggregation, and transport activity. Thus, NIRs provide a therapeutic strategy to dissolve cytoplasmic RBP aggregates and restore nuclear RBP localization and function. Indeed, Kapβ2 mitigated FUS loss of function in ALS-patient fibroblasts.

Kapβ2 must initially engage the PY-NLS to disaggregate RBP fibrils. This binding may enable Kapβ2 to extract individual RBPs from fibrils via entropic pulling. However, unlike Kapβ2, an antibody that binds the FUS PY-NLS is unable to dissolve FUS fibrils, arguing against simple versions of this model. The PrLD engages in cross-β contacts that maintain RBP fibrils (Murray et al., 2017). If the PY-NLS is not in the PrLD, then Kapβ2 rapidly disaggregates fibrils as with FUS, TAF15, and EWSR1. Kapβ2 binding to the PY-NLS may elicit a long-range allosteric conformational change in the PrLD that breaks cross-β fibril contacts. Alternatively, initial PY-NLS binding may enable Kapβ2 to engage secondary binding sites in the FUS PrLD and rapidly disrupt contacts that maintain fibril integrity (Yoshizawa et al., 2018).

If the PY-NLS is located in the PrLD, then Kapβ2 slowly disaggregates fibrils as with hnRNPA1 and hnRNPA2. Here, Kapβ2 binding to the PY-NLS breaks contacts that hold the fibril together. However, accessing the PY-NLS in hnRNPA1 or hnRNPA2 fibrils is likely more difficult because it is sequestered from solvent in the cross-β fibril core (Xiang et al., 2015). Nonetheless, thermal fluctuations may enable Kapβ2 to access the PY-NLS to slowly drive disaggregation of hnRNPA1 and hnRNPA2 fibrils.

Fibril-dissolution activity enables Kapβ2 to dissolve macroscopic hydrogels formed by RBP fibrils. Kapβ2 breaks multiple, weak hydrophobic contacts in hydrogels formed by FG-repeat rich nucleoporins to cross the nuclear pore during nuclear transport (Schmidt and Görlich, 2016). NIRs carry multiple binding-pockets for FG-repeat-rich nucleoporins (Schmidt and Görlich, 2016). This multivalency equips NIRs to break multiple transient intermolecular contacts between FG-repeat-rich nucleoporins, thus enabling specific and rapid passage across the nuclear pore. We suggest this multivalency also enables NIRs to rapidly break intermolecular contacts that maintain RBP liquids or RBP fibrils in gel phases (Monahan et al., 2017; Murray et al., 2017; Yoshizawa et al., 2018). This Kapβ2 activity weakens hydrogels formed by PrLD-containing RBPs without a functional PY-NLS, but when coupled to tight PY-NLS binding induces gel dissolution.

Kapβ2 inhibits seeded fibrillization of RBPs, which could prevent pathological spreading by prion-like conformers. Kapβ2 also dissolves RBP fibrils and reverses aberrant phase transitions of RBPs, which could be neuroprotective. Indeed, elevating Kapβ2 expression antagonized motor-neuron degeneration and extended lifespan in flies expressing ALS-linked FUS^{R521H}. Likewise, Kapβ2 antagonized muscle degeneration caused by MSP-linked hnRNPA2^{D290V} in fly. Increased NIR expression also buffers toxicity caused by C9orf72 dipeptide-repeat proteins (Kim and Taylor, 2017). In neurodegenerative diseases, NIRs may become overwhelmed and fail to counter excessive TDP-43, FUS or hnRNPA1 aggregation. Indeed, NIR expression is reduced in ALS/FTD patient brains (Kim and Taylor, 2017; Nishimura et al., 2010). Arginine methylation adjacent to the PY-NLS weakens interactions between Kapβ2 and FUS, and may reduce Kapβ2 activity in FTD (Hofweber et al., 2018). Moreover, Kapβ2 is sequestered in cytoplasmic inclusions in FTD, which may limit activity (Kim and Taylor, 2017). Thus, small molecules or other methods to increase NIR expression could be valuable therapeutics for several fatal neurodegenerative disorders.

Specific ALS-linked mutations such as FUS^{P525L}, FUS^{R495X}, and hnRNPA1^{P288S} also weaken Kapβ2 binding (Lee et al., 2006; Zhang and Chook, 2012). We envision engineering Kapβ2 with enhanced disaggregation activity against these mutant RBPs. Engineered Kapβ2 variants would bind to FUS^{P525L} with an affinity similar to the WT Kapβ2:FUS interaction and could be delivered as therapeutics for juvenile ALS caused by FUS^{P525L}. Likewise, small molecules that increase the affinity of Kapβ2 for FUS^{P525L} to WT levels could be therapeutic for ALS-FUS^{P525L}.

Finally, we have established that NLSs function as disaggregation signals. It will be enlightening to determine whether

(E) In ALS/FTD, nuclear RBPs with PrLDs mislocalize to the cytoplasm and upon stress localize to SGs where they undergo aberrant phase transitions to pathological fibrils. Upregulating Kapβ2 reverses aberrant phase transitions and solubilizes aggregated RBPs. Once solubilized, Kapβ2 transports RBPs back to the nucleus where Ran^{GTP} dissociates Kapβ2:RBP complexes enabling RBPs to perform nuclear functions and Kapβ2 to be recycled to catalyze further rounds of disaggregation.
See also Figure S7.

signal-dependent disaggregation activity extends to other transport factors that recognize short linear motifs such as signal-recognition particles (Jaru-Ampornpan et al., 2010), peroxisomal-import factors, tail-anchored-protein targeting factors, and nuclear-export factors. These agents may reverse aberrant phase transitions in diverse settings.

STAR★METHODS

Detailed methods are provided in the online version of this paper and include the following:

SUPPLEMENTAL INFORMATION

Supplemental Information includes seven figures, one table, and four movies and can be found with this article online at https://doi.org/10.1016/j.cell.2018.03.002.

AUTHOR CONTRIBUTIONS

DECLARATION OF INTERESTS

The authors declare no competing interests.

REFERENCES

Choi, S.H., Kim, Y.H., Hebisch, M., Sliwinski, C., Lee, S., D'Avanzo, C., Chen, H., Hooli, B., Asselin, C., Muffat, J., et al. (2014). A three-dimensional human neural cell culture model of Alzheimer's disease. Nature 515, 274–278.

Chook, Y.M., Jung, A., Rosen, M.K., and Blobel, G. (2002). Uncoupling Kap-beta2 substrate dissociation and ran binding. Biochemistry 41, 6955–6966.

Chou, C.C., Zhang, Y., Umoh, M.E., Vaughan, S.W., Lorenzini, I., Liu, F., Sayegh, M., Donlin-Asp, P.G., Chen, Y.H., Duong, D.M., et al. (2018). TDP-43 pathology disrupts nuclear pore complexes and nucleocytoplasmic transport in ALS/FTD. Nat. Neurosci. 21, 228–239.

Couthouis, J., Hart, M.P., Erion, R., King, O.D., Diaz, Z., Nakaya, T., Ibrahim, F., Kim, H.J., Mojsilovic-Petrovic, J., Panossian, S., et al. (2012). Evaluating the role of the FUS/TLS-related gene EWSR1 in amyotrophic lateral sclerosis. Hum. Mol. Genet. 21, 2899–2911.

Couthouis, J., Hart, M.P., Shorter, J., DeJesus-Hernandez, M., Erion, R., Oristano, R., Liu, A.X., Ramos, D., Jethava, N., Hosangadi, D., et al. (2011). A yeast functional screen predicts new candidate ALS disease genes. Proc. Natl. Acad. Sci. USA 108, 20881–20890.

Daigle, J.G., Lanson, N.A., Jr., Smith, R.B., Casci, I., Maltare, A., Monaghan, J., Nichols, C.D., Kryndushkin, D., Shewmaker, F., and Pandey, U.B. (2013). RNA-binding ability of FUS regulates neurodegeneration, cytoplasmic misloc-alization and incorporation into stress granules associated with FUS carrying ALS-linked mutations. Hum. Mol. Genet. 22, 1193–1205.

Franzmann, T.M., Jahnel, M., Pozniakovsky, A., Mahamid, J., Holehouse, A.S., Nüske, E., Richter, D., Baumeister, W., Grill, S.W., Pappu, R.V., et al. (2018). Phase separation of a yeast prion protein promotes cellular fitness. Science 359, eaao5654.

Harrison, A.F., and Shorter, J. (2017). RNA-binding proteins with prion-like do-mains in health and disease. Biochem. J. 474, 1417–1438.

Hofweber, M., Hutten, S., Bourgeois, B., Spreitzer, E., Niedner-Boblenz, A., Schifferer, M., Simons, M., Ruepp, M.-D., Niessing, D., Madl, T., et al. (2018). Phase separation of FUS is suppressed by its nuclear import receptor and arginine methylation. Cell 173. Published online April 19, 2018. https://doi.org/10.1016/j.cell.2018.03.004.

Jackrel, M.E., DeSantis, M.E., Martinez, B.A., Castellano, L.M., Stewart, R.M., Caldwell, K.A., Caldwell, G.A., and Shorter, J. (2014). Potentiated Hsp104 var-iants antagonize diverse proteotoxic misfolding events. Cell 156, 170–182.

Jäkel, S., Mingot, J.M., Schwarzmaier, P., Hartmann, E., and Görlich, D. (2002). Importins fulfil a dual function as nuclear import receptors and cyto-plasmic chaperones for exposed basic domains. EMBO J. 21, 377–386.

Jaru-Ampornpan, P., Shen, K., Lam, V.Q., Ali, M., Doniach, S., Jia, T.Z., and Shan, S.O. (2010). ATP-independent reversal of a membrane protein aggre-gate by a chloroplast SRP subunit. Nat. Struct. Mol. Biol. 17, 696–702.

Johnson, B.S., Snead, D., Lee, J.J., McCaffery, J.M., Shorter, J., and Gitler, A.D. (2009). TDP-43 is intrinsically aggregation-prone, and amyotrophic lateral sclerosis-linked mutations accelerate aggregation and increase toxicity. J. Biol. Chem. 284, 20329–20339.

Ju, S., Tardiff, D.F., Han, H., Divya, K., Zhong, Q., Maquat, L.E., Bosco, D.A., Hayward, L.J., Brown, R.H., Jr., Lindquist, S., et al. (2011). A yeast model of FUS/TLS-dependent cytotoxicity. PLoS Biol. 9, e1001052.

Kim, H.J., Kim, N.C., Wang, Y.D., Scarborough, E.A., Moore, J., Diaz, Z., MacLea, K.S., Freibaum, B., Li, S., Molliex, A., et al. (2013). Mutations in prion-like domains in hnRNPA2B1 and hnRNPA1 cause multisystem protein-opathy and ALS. Nature 495, 467–473.

Kim, H.J., and Taylor, J.P. (2017). Lost in transportation: nucleocytoplasmic transport defects in ALS and other neurodegenerative diseases. Neuron 96, 285–297.

Kim, Y.H., Choi, S.H., D'Avanzo, C., Hebisch, M., Sliwinski, C., Bylykbashi, E., Washicosky, K.J., Klee, J.B., Brüstle, O., Tanzi, R.E., and Kim, D.Y. (2015). A 3D human neural cell culture system for modeling Alzheimer's disease. Nat. Protoc. 10, 985–1006.

Lanson, N.A., Jr., Maltare, A., King, H., Smith, R., Kim, J.H., Taylor, J.P., Lloyd, T.E., and Pandey, U.B. (2011). A Drosophila model of FUS-related neurode-generation reveals genetic interaction between FUS and TDP-43. Hum. Mol. Genet. 20, 2510–2523.

Lee, B.J., Cansizoglu, A.E., Süel, K.E., Louis, T.H., Zhang, Z., and Chook, Y.M. (2006). Rules for nuclear localization sequence recognition by karyopherin beta 2. Cell 126, 543–558.

Levental, I., Georges, P.C., and Janmey, P.A. (2007). Soft biological materials and their impact on cell function. Soft Matter 3, 299–306.

Lin, Y., Protter, D.S., Rosen, M.K., and Parker, R. (2015). Formation and matu-ration of phase-separated liquid droplets by RNA-binding proteins. Mol. Cell 60, 208–219.

March, Z.M., King, O.D., and Shorter, J. (2016). Prion-like domains as epige-netic regulators, scaffolds for subcellular organization, and drivers of neurode-generative disease. Brain Res. 1647, 9–18.

Milles, S., Huy Bui, K., Koehler, C., Eltsov, M., Beck, M., and Lemke, E.A. (2013). Facilitated aggregation of FG nucleoporins under molecular crowding conditions. EMBO Rep. 14, 178–183.

Molliex, A., Temirov, J., Lee, J., Coughlin, M., Kanagaraj, A.P., Kim, H.J., Mittag, T., and Taylor, J.P. (2015). Phase separation by low complexity do-mains promotes stress granule assembly and drives pathological fibrillization. Cell 163, 123–133.

Monahan, Z., Ryan, V.H., Janke, A.M., Burke, K.A., Rhoads, S.N., Zerze, G.H., O'Meally, R., Dignon, G.L., Conicella, A.E., Zheng, W., et al. (2017). Phosphor-ylation of the FUS low-complexity domain disrupts phase separation, aggre-gation, and toxicity. EMBO J. 36, 2951–2967.

Murakami, T., Qamar, S., Lin, J.Q., Schierle, G.S., Rees, E., Miyashita, A., Costa, A.R., Dodd, R.B., Chan, F.T., Michel, C.H., et al. (2015). ALS/FTD mu-tation-induced phase transition of FUS liquid droplets and reversible hydrogels into irreversible hydrogels impairs RNP granule function. Neuron 88, 678–690.

Murray, D.T., Kato, M., Lin, Y., Thurber, K.R., Hung, I., McKnight, S.L., and Tycko, R. (2017). Structure of FUS protein fibrils and its relevance to self-as-sembly and phase separation of low-complexity domains. Cell 171, 615–627.

Nishimura, A.L., Zupunski, V., Troakes, C., Kathe, C., Fratta, P., Howell, M., Gallo, J.M., Hortobágyi, T., Shaw, C.E., and Rogelj, B. (2010). Nuclear import impairment causes cytoplasmic trans-activation response DNA-binding pro-tein accumulation and is associated with frontotemporal lobar degeneration. Brain 133, 1763–1771.

Patel, A., Lee, H.O., Jawerth, L., Maharana, S., Jahnel, M., Hein, M.Y., Stoynov, S., Mahamid, J., Saha, S., Franzmann, T.M., et al. (2015). A liquid-to-solid phase transition of the ALS protein FUS accelerated by disease muta-tion. Cell 162, 1066–1077.

Ran, F.A., Hsu, P.D., Wright, J., Agarwala, V., Scott, D.A., and Zhang, F. (2013). Genome engineering using the CRISPR-Cas9 system. Nat. Protoc. 8, 2281–2308.

Rodell, C.B., Kaminski, A.L., and Burdick, J.A. (2013). Rational design of network properties in guest-host assembled and shear-thinning hyaluronic acid hydrogels. Biomacromolecules 14, 4125–4134.

Schmidt, H.B., and Görlich, D. (2016). Transport selectivity of nuclear pores, phase separation, and membraneless organelles. Trends Biochem. Sci. 41, 46–61.

Shorter, J. (2011). The mammalian disaggregase machinery: Hsp110 syner-gizes with Hsp70 and Hsp40 to catalyze protein disaggregation and reactiva-tion in a cell-free system. PLoS ONE 6, e26319.

Shorter, J. (2016). Engineering therapeutic protein disaggregases. Mol. Biol. Cell 27, 1556–1560.

Sun, Z., Diaz, Z., Fang, X., Hart, M.P., Chesi, A., Shorter, J., and Gitler, A.D. (2011). Molecular determinants and genetic modifiers of aggregation and toxicity for the ALS disease protein FUS/TLS. PLoS Biol. 9, e1000614.

Vance, C., Rogelj, B., Hortobagyi, T., De Vos, K.J., Nishimura, A.L., Sreed-haran, J., Hu, X., Smith, B., Ruddy, D., Wright, P., et al. (2009). Mutations in FUS, an RNA processing protein, cause familial amyotrophic lateral sclerosis type 6. Science 323, 1208–1211.

Wang, W.Y., Pan, L., Su, S.C., Quinn, E.J., Sasaki, M., Jimenez, J.C., Mackenzie, I.R., Huang, E.J., and Tsai, L.H. (2013). Interaction of FUS and HDAC1 regulates DNA damage response and repair in neurons. Nat. Neurosci. 16, 1383–1391.

Xiang, S., Kato, M., Wu, L.C., Lin, Y., Ding, M., Zhang, Y., Yu, Y., and McKnight, S.L. (2015). The LC domain of hnRNPA2 adopts similar conformations in hy-drogel polymers, liquid-like droplets, and nuclei. Cell 163, 829–839.

Yoshizawa, T., Ali, R., Jiou, J., Fung, H.-Y.J., Burke, K.A., Lin, Y., Peeples, W.B., Kim, S.J., Saltzberg, D., Soniat, M., et al. (2018). Nuclear import receptor inhibits phase separation of FUS through binding to multiple sites. Cell 173. Published online April 19, 2018. https://doi.org/10.1016/j.cell.2018.03.003.

Zhang, Z.C., and Chook, Y.M. (2012). Structural and energetic basis of ALS-causing mutations in the atypical proline-tyrosine nuclear localization signal of the fused in sarcoma protein (FUS). Proc. Natl. Acad. Sci. USA 109, 12017–12021.

Zhang, Z.C., Satterly, N., Fontoura, B.M., and Chook, Y.M. (2011). Evolu-tionary development of redundant nuclear localization signals in the mRNA export factor NXF1. Mol. Biol. Cell 22, 4657–4668.

STAR★METHODS

KEY RESOURCES TABLE

REAGENT or RESOURCE	SOURCE	IDENTIFIER
Antibodies		
Rabbit monoclonal anti-HA (C29F4)	Cell Signaling	Cat# 3724; RRID: AB_1549585
Rabbit polyclonal anti-eIF4G (H300)	Santa Cruz	Cat# sc-11373; RRID: AB_2095750
Rabbit polyclonal anti-GFP (FL)	Santa Cruz	Cat# sc-8334 RRID:AB_641123
Rabbit polyclonal anti-Actin antibody	Santa Cruz	Cat# sc-1616-R; RRID: AB_630834
Rabbit polyclonal anti-GAPDH antibody	Sigma-Aldrich	Cat# G9545 RRID:AB_796208
Mouse monoclonal anti-G3BP1	BD Biosciences	Cat# 611126; RRID: AB_398437
Mouse monoclonal anti-Flag (M2)	Sigma-Aldrich	Cat# F3165; RRID:AB_259529
Mouse monoclonal anti-hnRNPA2B1 (EF-67)	Santa Cruz	Cat# sc-53531 RRID:AB_2248245
Donkey anti-Rabbit IgG Secondary Antibody, Alexa Fluor 594	Thermo Fisher Scientific	Cat# R37119 RRID:AB_2556547
Donkey anti-Rabbit IgG (H+L) Secondary Antibody, Alexa Fluor 647	Molecular Probes	Cat# A31573 RRID:AB_2536183
Donkey anti-Mouse IgG Secondary Antibody, Alexa Fluor 594	Thermo Fisher Scientific	Cat# R37115 RRID:AB_2556543
Donkey anti-Mouse IgG (H+L) Secondary Antibody, Alexa Fluor 647	Molecular Probes	Cat# A31571 RRID:AB_162542
Alexa Fluor 647 Phalloidin	Invitrogen	Cat# A22287
Texas Red-X Phalloidin	Invitrogen	Cat# T7471
Anti-GFP antibody	Santa Cruz Biotechnology	Cat# sc-9996
Anti-FUS rabbit polyclonal antibody	Bethyl	Cat# A300-302A
Anti-FUS rabbit polyclonal antibody	Novus	Cat# NB100-562
Anti-Kapβ2 monoclonal antibody	Novus	Cat# NB600-1397
Fluorescently labeled anti-mouse secondary antibodies	Li-Cor	Cat# 926-32210
Fluorescently labeled anti-rabbit secondary antibodies	Li-Cor	Cat# 926-68071
Rabbit polyclonal anti-FUS	Proteintech	Cat# 11570-1-AP
Cy3 AffiniPure Donkey Anti-Mouse IgG (H+L)	Jackson immunoresearch	Cat# 715-165-151
Bacterial and Virus Strains		
E. coli BL21 DE3 cells	Agilent	Cat# 200131
E. coli BL21 DE3 (RIL) cells	Agilent	Cat# 230245
E. coli BL21 Star cells	Invitrogen	Cat# C6010-03
Chemicals, Peptides, and Recombinant Proteins		
AcTEV Protease	Invitrogen	Cat# 12575015
Firefly luciferase	Sigma	Cat# L-9506
Hsc70	Enzo Life Sciences	Cat# ADI-SPP-751
Hdj1	Enzo Life Sciences	Cat# ADI-SPP-400
Creatine kinase	Roche	Cat# 12003920
Sulfo-NHS-LC-Biotin	Thermofisher	Cat# 21335
Pierce NeutrAvidin UltraLink Resin	Thermofisher	Cat# 53150
Ni-NTA agarose	QIAGEN	Cat# 30230
Lipofectamine LTX with Plus Reagent	Invitrogen	Cat# 15338100
FuGENE 6	Promega	Cat# E2691
Sodium Arsenite Solution	Sigma Aldrich	Cat# 35000-1L-R
ProLong Gold Antifade Mountant with DAPI	Thermo Fisher Scientific	Cat# P36931

(Continued on next page)

Continued

REAGENT or RESOURCE	SOURCE	IDENTIFIER
ProLong Diamond Antifade Mountant with DAPI	Thermo Fisher Scientific	Cat# P36971
20% paraformaldehyde	Electron Microscopy Science	Cat# 15713-S
Protease inhibitor	Roche	Cat# 11697498001
EDTA-free Protease Inhibitor Cocktail	Roche	Cat# 11873580001
NuPAGE LDS sample buffer (4X)	Thermo Fisher Scientific	Cat# NP0007
Sodium Arsenite	Sigma-Aldrich	Cat# S7400
ProLong Gold Antifade Mountant	Thermo Fisher Scientific	Cat# P36934
Dapi (SelectFX Nuclear Labeling Kit)	Thermo Fisher Scientific	Cat# S33025
20% paraformaldehyde	Thermo Fisher Scientific	Cat# 50980493
TRIzol RNA Isolation Reagents	Thermo Fisher Scientific	Cat# 10296-010
iTaq Universal SYBR Green Supermix	BioRad	Cat# 1725122
high-glucose DMEM/F12 medium	Thermo Fisher Scientific	Cat# 11320082
heparin	StemCell Technologies	Cat# 07980
B27 neural supplement	Thermo Fisher Scientific	Cat# 175004044
human Epidermal Growth Factor	Sigma-Aldrich	Cat# E9644
basic human Fibroblast Growth Factor	Stemgent	Cat# 03-0002
Matrigel	BD Biosciences	Cat# 356234
Fetal Bovine Serum	Sigma-Aldrich	Cat# F0926
penicillin/streptomycin	Thermo Fisher Scientific	Cat# 15140122
Critical Commercial Assays		
CytoTox-ONE kit	Promega	Cat# G7890
Rat Neural Stem Cell Nucleofector Kit (25 RCT)	Lonza	Cat# VPG-1005
High-Capacity cDNA Reverse Transcription Kit with RNase Inhibitor	Thermo Fisher Scientific	Cat# 4374966
QuikChange Site-Directed Mutagenesis Kit	Agilent	Cat# 210518
Experimental Models: Cell Lines		
Human: HEK293T	ATCC	Cat# CRL-3216
Human: HeLa	ATCC	Cat# CCL-2; RRID:CVCL_0030
ReNcell VM Human Neural Progenitor Cell Line	Millipore Sigma	Cat# SCC008
Experimental Models: Organisms/Strains		
BY4741 yeast (*MATa his3 leu2 met15 ura3*)	Sun et al., 2011	N/A
D. melanogaster: UAS-hnRNPA2 WT	Kim et al., 2013	N/A
D. melanogaster: UAS-hnRNPA2 D290V	Kim et al., 2013	N/A
D. melanogaster: UAS-GFP-Kapβ2	This paper	N/A
D. melanogaster: UAS-LacZ; P{w[+mC] = UAS-lacZ.B}Bg4-2-4b	Bloomington Drosophila Stock Center	BDSC: 1777
D. melanogaster: RNAi of Tnpo (http://flybase.org/reports/FBgn0024921); P{KK108990}	Vienna Drosophila Resource Center	VDRC: 105181; FlyBase: FBgn0033507
D. melanogaster: RNAi-TK; P{KK108990}	Vienna Drosophila Resource Center	VDRC: 60100
HA-FUSR521H	Lanson et al., 2011	N/A
UAS-Kaβ2 RNAi	Vienna Drosophila RNAi Center	Stock # v6543 and v6544
UAS-Kapβ2 overexpression	This paper	N/A
Oligonucleotides		
See Table S1 for Primers	IDT	N/A
Recombinant DNA		
GST-TEV-FUS	Sun et al., 2011	N/A
GST-TEV-His-FUS	This paper	N/A

Continued

REAGENT or RESOURCE	SOURCE	IDENTIFIER
GST-TEV-FUS$^{1-214}$	This paper	N/A
GST-TEV- FUS^{R234L}	Sun et al., 2011	N/A
GST-TEV-FUS^{R495X}	Sun et al., 2011	N/A
GST-TEV-FUS^{P525L}	Sun et al., 2011	N/A
GST-TEV-FUS^{R521C}	Sun et al., 2011	N/A
GST-TEV-FUS^{H517Q}	Sun et al., 2011	N/A
GST-TEV-FUS^{R521H}	Sun et al., 2011	N/A
GST-TEV-FUS$^{\Delta498-526}$ (FUS$^{\Delta NLS}$)	This paper	N/A
GST-TEV-TDP-43,	Johnson et al., 2009	N/A
GST-TEV-TDP-43^{Q331K}	Johnson et al., 2009	N/A
GST-TEV-TDP-43$^{188-414}$	This paper	N/A
GST-TEV-TDP-43$^{\Delta79-98}$	This paper	N/A
GST-TEV-hnRNPA1	Kim et al., 2013	N/A
GST-TEV-hnRNPA1^{D262N}	Kim et al., 2013	N/A
GST-TEV-hnRNPA1^{D262V}	Kim et al., 2013	N/A
GST-TEV-hnRNPA1$^{G274A:P288A:Y289A}$	This paper	N/A
GST-TEV-hnRNPA1$^{\Delta268-289}$ (hnRNPA1$^{\Delta NLS}$)	This paper	N/A
GST-TEV-hnRNPA2	Kim et al., 2013	N/A
GST-TEV-hnRNPA2^{D290V}	Kim et al., 2013	N/A
GST-TEV-hnRNPA2$^{\Delta293-319}$ (hnRNPA2$^{\Delta NLS}$)	This paper	N/A
GST-TEV-TAF15	Couthouis et al., 2011	N/A
GST-TEV-TAF15^{G391E}	Couthouis et al., 2011	N/A
GST-TEV-TAF15^{R408C}	Couthouis et al., 2011	N/A
GST-TEV-TAF15$^{\Delta572-592}$ (TAF15$^{\Delta NLS}$)	This paper	N/A
GST-TEV-EWSR1	Couthouis et al., 2011	N/A
GST-TEV-EWSR1^{G511A}	Couthouis et al., 2011	N/A
GST-TEV-EWSR1^{P552L}	Couthouis et al., 2011	N/A
GST-TEV-EWSR1$^{\Delta630-655}$ (EWSR1$^{\Delta NLS}$)	This paper	N/A
Hsp104^{A503S}	Jackrel et al., 2014	N/A
Apg2	Shorter, 2011	N/A
Sse1	Shorter, 2011	N/A
Ssa1	Shorter, 2011	N/A
Ydj1	Shorter, 2011	N/A
GST-TEV-Kapβ2	Lee et al., 2006	N/A
GST-TEV-Kapβ2$^{W460A:W730A}$	Lee et al., 2006	N/A
GST-TEV-Kapβ2^{TL}	Lee et al., 2006	N/A
Impα	Zhang et al., 2011	N/A
Kapβ1	Zhang et al., 2011	N/A
Ran^{Q69L}	Zhang et al., 2011	N/A
pDONR221-Kapβ2	Gideon Dreyfuss	N/A
pAG413Gal-Kapβ2	This paper	N/A
pYES2CT/GFP-FUS	Gregory Petsko; Ju et al., 2011	N/A
p426CUP-GFP-FUS	This paper	N/A
pAG413Gal-Kapβ2$^{W460A:W730A}$	This paper	N/A
pYES2CT/GFP-FUS^{R495X}	This paper	N/A
pYES2CT/GFP-FUS^{R521C}	This paper	N/A
pYES2CT/GFP-FUS^{R521H}	This paper	N/A
pYES2CT/GFP-FUS^{P525L}	This paper	N/A

Continued

REAGENT or RESOURCE	SOURCE	IDENTIFIER
pYES2CT/GFP-EWSR1	This paper	N/A
pYES2CT/GFP-hnRNPA1	This paper	N/A
pYES2CT/GFP-hnRNPA2	This paper	N/A
pUAST-Kapβ2	This paper	N/A
pUASTattB-wild type GFP-Karyopherin β2	This paper	N/A
Plasmid: HA-FUS WT	Vance et al., 2009	N/A
Plasmid: HA-FUS R518K	Daigle et al., 2013	N/A
Plasmid: HA-FUS R521C	Vance et al., 2009	N/A
Plasmid: HA-FUS R521H	Vance et al., 2009	N/A
Plasmid: HA-FUS ΔNLS	This paper	N/A
Plasmid: GFP-Kapβ2^{WT}	This paper	N/A
Plasmid: GFP-Kapβ2$^{W460A:W730A}$	This paper	N/A
Plasmid: GFP-Kapβ2^{TL}	This paper	N/A
Plasmid: pGFPmax	Lonza	Cat# VPG-1005
Plasmid: pSpCas9(BB)-2A-GFP (PX458)	Ran et al., 2013	Addgene Cat# 48138
Software and Algorithms		
Image Studio	LI-COR	https://www.licor.com/bio/products/software/image_studio_lite/?utm_source=BIO+Blog&utm_medium=28Aug13post&utm_content=ISLite1&utm_campaign=ISLite; RRID: SCR_014211
ImageJ	NIH	https://imagej.nih.gov/ij/; RRID: SCR_003073
GraphPad Prism	GraphPad Software Inc	https://www.graphpad.com/scientific-software/prism/; RRID: SCR_002798

CONTACT FOR REAGENT AND RESOURCE SHARING

Further information and requests for resources and reagents should be directed to and will be fulfilled by the Lead Contact James Shorter (jshorter@pennmedicine.upenn.edu).

EXPERIMENTAL MODEL AND SUBJECT DETAIL

Yeast Strains and Media

BY4741 yeast cells (*MATa his3 leu2 met15 ura3*) were grown in rich media (YPD) or in synthetic media lacking L-histidine and uracil and containing 2% glucose (SD/-His-Ura), raffinose (SRaf/-His-Ura), or galactose (SGal/-His-Ura).

Cell Culture

Human HEK293T cells (female) and HeLa cells (female) were grown in Dulbecco's modified Eagle's medium (DMEM) supplemented with 10% fetal bovine serum (FBS), 1% penicillin/streptomycin, and 1% L-glutamate.

Primary and immortalized fibroblasts from 3 healthy individuals (one 49-year-old female, one 50-year old male, and one 60-year old male) and 3 ALS patients (one 36-year old female, one 41-year old female, and one 70-year old male) harboring a FUS R521H mutation were grown in high-glucose DMEM/F12 (Thermofisher Scientific) supplemented with 20% (vol/vol) tetracycline-free FBS (Sigma), 1% (vol/vol) penicillin/streptomycin (Thermofisher Scientific). Fibroblasts were derived from skin biopsies after patients provided written informed consent at the VIB-KU Leuven and all experimental procedures were approved by the Institutional Review Board at the Massachusetts General Hospital.

Isogenic ReNcell VM human neural progenitors (male) were maintained in high-glucose DMEM/F12 (ThermoFisher Scientific) media supplemented with 2 μg.mL^{-1} heparin (StemCell Technologies, #07980), 2% (v/v) B27 neural supplement (ThermoFisher Scientific, #175004044), 20 μg.mL^{-1} hEGF (Sigma-Aldrich, #E9644), 20 μg.mL^{-1} bFGF (Stemgent, #03-0002) and 1% penicillin/streptomycin (ThermoFisher Scientific) and were plated onto Matrigel (BD Biosciences)-coated cell culture 24-well format coverslips.

Drosophila maintenance, strains, and genetics

Fly lines were maintained on standard food using standard methods as described previously (Lanson et al., 2011). UAS-Kaβ2 RNAi strains (stock # v6543 and v6544) were obtained from the Vienna *Drosophila* Resource Centre (VDRC). UAS-HA-FUS strains have been previously described (Lanson et al., 2011). UAS-Kapβ2 strains were made using random integration of plasmids pUAST-Kaβ2. Microinjection of these plasmids was performed by BestGene.

Flies expressing wild-type hnRNPA2 and D290V mutant form of hnRNPA2 have been described previously (Kim et al., 2013). The GFP-tagged wild-type Karyopherin-β2 cDNAs were subcloned into the pUASTattB plasmid, using restriction sites NotI and XbaI, creating pUASTattB-wild-type GFP-Karyopherin-β2. Flies carrying pUASTattB transgenes were generated by a standard injection and QC31 integrase-mediated transgenesis technique. To express a transgene in muscles, Mhc-Gal4 was used (Kim et al., 2013). All *Drosophila* stocks were maintained in a 25°C incubator with a 12h day/night cycle.

METHODS DETAILS

Protein purification

All proteins were expressed and purified from *E. coli* BL21-CodonPlus(DE3)-RIL cells (Agilent) and purified under native conditions unless otherwise noted. RBP expression constructs were generated in pGST-Duet to contain a TEV-cleavable site, resulting in a GST-TEV-RBP construct. GST-TEV-FUS, GST-TEV-His-FUS, GST-TEV-FUS$^{1-214}$, GST-TEV-FUS^{R234L}, GST-TEV-FUS^{R495X}, GST-TEV-FUS^{P525L}, GST-TEV-FUS^{R521C}, GST-TEV-FUS^{H517Q}, GST-TEV-FUS^{R521H}, and GST-TEV-FUS$^{\Delta498-526}$ (FUS$^{\Delta NLS}$) were purified as described (Sun et al., 2011). *E. coli* cells were lysed by sonication on ice in PBS with protease inhibitors (cOmplete, EDTA-free, Roche Applied Science). The protein was purified over Glutathione Sepharose 4 Fast Flow (GE Healthcare) and eluted from the beads using 50mM Tris-HCl, pH 8, 20 mM trehalose, and 20mM glutathione. GST-TEV-TDP-43, GST-TEV-TDP-43^{Q331K}, GST-TEV-TDP-43$^{188-414}$, and GST-TEV-TDP-43$^{\Delta79-98}$ were purified as described (Johnson et al., 2009), GST-TEV-hnRNPA1, GST-TEV-hnRNPA1^{D262N}, GST-TEV-hnRNPA1^{D262V}, GST-TEV-hnRNPA1$^{G274A:P288A:Y289A}$, GST-TEV-hnRNPA1$^{\Delta268-289}$ (hnRNPA1$^{\Delta NLS}$), GST-TEV-hnRNPA2, GST-TEV-hnRNPA2^{D290V}, and GST-TEV-hnRNPA2$^{\Delta293-319}$ (hnRNPA2$^{\Delta NLS}$) were purified as described (Kim et al., 2013). For GST-TEV-TDP-43, GST-TEV-hnRNPA1, and GST-TEV-hnRNPA2, *E. coli* cells were lysed by sonication on ice in 40mM HEPES-KOH (pH 7.4), 5mM EDTA, 300mM KCl, 1mM DTT, 5% glycerol, 5 μM pepstatin, 10mg/Liter RNase A and protease inhibitors (cOmplete, EDTA-free, Roche Applied Science). The protein was purified over Glutathione Sepharose 4 Fast Flow (GE Healthcare) and eluted from the beads using 40mM HEPES-KOH (pH 7.4), 150mM NaCl, 5% glycerol, and 20mM reduced glutathione. GST-TEV-TAF15, GST-TEV-TAF15^{G391E}, GST-TEV-TAF15^{R408C}, GST-TEV-TAF15$^{\Delta572-592}$ (TAF15$^{\Delta NLS}$) were purified as described (Couthouis et al., 2011). GST-TEV-EWSR1, GST-TEV-EWSR1^{G511A}, GST-TEV-EWSR1^{P552L}, and GST-TEV-EWSR1$^{\Delta630-655}$ (EWSR1$^{\Delta NLS}$) were purified as described (Couthouis et al., 2012). These proteins were overexpressed in *E. coli* BL21 Star (Invitrogen) and eluted from the glutathione sepharose with 50mM Tris–HCl, pH 7.4, 100mM potassium acetate, 200mM trehalose, 0.5mM ethylenediaminetetraacetic acid (EDTA) and 20mM glutathione.

Hsp104 and Hsp104^{A503S} were purified as untagged proteins as described (Jackrel et al., 2014). Cells were harvested, lysed with lysis buffer (50mM Tris-HCl, pH 8.0, 10mM MgCl$_2$, 2.5% glycerol, 2mM β-mercaptoethanol) supplemented with protease inhibitors, and the protein was purified using Affi-Gel Blue Gel (Bio-Rad). The protein was eluted with elution buffer (50mM Tris-HCl, pH 8.0, 1M KCl, 10mM MgCl$_2$, 2.5% glycerol, 2mM β-mercaptoethanol) and further purified by ResourceQ anion exchange chromatography using running buffer Q (20mM Tris-HCl, pH 8.0, 0.5mM EDTA, 5mM MgCl$_2$, 50mM NaCl) and eluted with a linear gradient of buffer Q+ (20mM Tris-HCl, pH 8.0, 0.5mM EDTA, 5mM MgCl$_2$, 1M NaCl). Immediately before loading the column, the protein was diluted to a final concentration of 10% in buffer Q supplemented to 150mM NaCl and loaded onto the column.

Apg2, Sse1, Ssa1, and Ydj1 were purified as described (Shorter, 2011). Briefly, Apg2 was purified via sequential DEAE–Sepharose and DMAE–Sepharose anion exchange chromatography. Both anion-exchange steps were performed in 25mM HEPES–KOH, pH 7.6, 50mM KCl, 1mM EDTA, 10mM β-mercaptoethanol, and 10% glycerol. Apg2 was eluted with a linear 55–500 mM KCl gradient. To remove further impurities, purified fractions were pooled, concentrated by ammonium sulfate precipitation and fractionated via Sephacryl 300 gel filtration in 25mM HEPES–KOH, pH 7.6, 50mM KCl, 5mM MgCl$_2$, plus 5% glycerol. Sse1 was purified with a similar protocol except that the gel filtration step was replaced by a hydroxyapatite column, equilibrated in 10mM K$_x$H$_y$PO$_4$, pH 7.6, 5mM MgCl$_2$, and 5% glycerol. Sse1 was eluted with a linear 10–500 mM phosphate gradient.

Ssa1 were expressed as an N-terminally His-tagged protein. Cells were lysed by sonication in 40mM HEPES-KOH. pH 7.4, 500mM KCl, 20mM MgCl$_2$, 5% (w/v) glycerol, 20mM imidazole, 5mM ATP, 2mM β-mercaptoethanol, 5μM pepstatin A, and Complete protease inhibitor cocktail. Cell debris was removed by centrifugation (40,000 g, 20min, 4°C), and the supernatant applied to Ni-NTA agarose. The column was then washed with 25 volumes of WB (40mM HEPES-KOH, pH 7.4, 150mM KCl, 20mM MgCl$_2$, 5% (w/v) glycerol, 20mM imidazole, 5mM ATP, and 2mM β-mercaptoethanol), 5 volumes of WB plus 1M KCl, and 25 volumes of WB. Protein was eluted with WB plus 350mM imidazole, and purified further by sucrose gradient (5%–30% w/v in WB) velocity sedimentation. Peak fractions were collected and exchanged into 40mM HEPES-KOH, pH 7.4, 150mM KCl, 20mM MgCl$_2$, 10% (w/v) glycerol, 5mM ATP and 1mM DTT. The His-tag was then removed with His-TEV (Invitrogen), and any uncleaved protein and His-TEV were depleted with Ni-NTA.

Ydj1 was overexpressed in BL21 (DE3) *E. coli* cells, which were lysed in buffer containing 20mM MOPS, pH 7.5, 0.5mM EDTA, 10mM DTT, and 0.5 mM PMSF (phenylmethylsulfonyl fluoride). Cleared lysate was loaded onto a DE52 column (Whatman)

equilibrated with buffer containing 20mM MOPS, pH 7.5, 0.5mM EDTA, 10mM DTT, and 0.5 mM PMSF. Ydj1 was eluted with a 0-300 mM NaCl gradient. Peak fractions containing Ydj1 were pooled, dialyzed against buffer containing 5mM potassium phosphate, pH 7.0, and 10mM DTT and then purified over a hydroxyapatite column. The protein was then eluted with a linear 5-400 mM potassium phosphate gradient and dialyzed against buffer containing 10mM HEPES-KOH, pH 7.4, 50mM NaCl, 10mM DTT, and 10% glycerol.

Kapβ2 and Kapβ2$^{W460A:W730A}$ were purified as described (Lee et al., 2006). Impα and Kapβ1 were purified as described (Zhang et al., 2011). GST-Importins were expressed individually in BL21 (DE3) *E. coli* cells, which were lysed in buffer containing 50mM Tris-HCl, pH 7.5, 200mM NaCl, 20% (v/v) glycerol, 2mM DTT, 1mM EDTA, and protease inhibitors. GST-Importins were then purified by affinity chromatography using GSH Sepharose beads (GE Healthcare, UK), eluted, cleaved with TEV protease, and further purified by ion-exchange and gel filtration chromatography in buffer (20mM HEPES-NaOH, pH 7.4, 200mM NaCl, 2mM DTT, 2mM magnesium acetate, 10% glycerol, and 1mM EGTA).

Ran^{Q69L} was purified and loaded with GTP or GDP as described (Zhang et al., 2011). The protein was expressed in *E. coli* BL21-DE3 and purified from a French press lysate in buffer (20 mM HEPES, pH 7.3, 110 mM potassium acetate, 5 mM magnesium acetate, 1 mM EGTA, 10 mM DTT, 20% glycerol) containing 10 μM GDP, via sequential Q-Hi-Trap, SP Hi-Trap and Superdex-75 chromatography (Pharmacia). Hsc70 and Hdj1 were from Enzo Life Sciences. Anti-FUS rabbit polyclonal antibody (NB100-562) was from Novus. HDAC1 was from BPS Bioscience. TEV protease was from Invitrogen. Firefly luciferase was from Sigma.

Spontaneous fibril assembly—Figure 1, Figure S1

Spontaneous FUS (and disease-linked variant) fibrillization (i.e., in the absence of preformed fibril seeds) was initiated by addition of TEV protease to GST-TEV-FUS (5μM) in FUS assembly buffer (50mM Tris-HCl, pH 8, 200mM trehalose, 1mM DTT, and 20mM glutathione) (Couthouis et al., 2011, 2012; Sun et al., 2011). Spontaneous FUS fibrillization reactions were incubated at 25°C for 90min without agitation at which time fibrillization was complete with ∼100% of FUS in the aggregated state. Spontaneous EWSR1, TAF15, and TDP-43 (and disease-linked variants) fibrillization was initiated by addition of TEV protease to GST-TEV-RBP (5μM) in ETT assembly buffer (50mM Tris-HCl, pH 7.4, 200mM trehalose, 100mM potassium acetate, 0.5mM EDTA, and 20mM glutathione). Spontaneous EWSR1, TAF15, TDP-43 fibrillization reactions were incubated at 25°C for 90 min with agitation at 700rpm in an Eppendorf Thermomixer at which time fibrillization was complete with ∼100% of the RBP in the aggregated state. TDP-43^{ΔNLS} took longer to fibrillize, and thus was incubated at 25°C for 16h with agitation at 700rpm at which time fibrillization was complete with ∼100% of the TDP-43^{ΔNLS} in the aggregated state. For hnRNPA1 and hnRNPA2 fibrillization (and disease-linked variants), GST-TEV-hnRNPA1 or GST-TEV-hnRNPA2 (5 μM) were incubated with TEV protease in A1 assembly buffer (40mM HEPES-NaOH, pH 7.4, 150mM NaCl, 5% glycerol, 1mM DTT, and 20 mM glutathione). HnRNPA1 and hnRNPA2 fibrillization reactions were incubated at 25°C for 16h with agitation at 1,200rpm in an Eppendorf Thermomixer at which time fibrillization was complete with ∼100% of the hnRNP in the aggregated state. No RBP fibrillization occurs in the absence of TEV protease (Couthouis et al., 2011, 2012; Kim et al., 2013; Sun et al., 2011). Spontaneous fibrillization reactions were performed in the presence or absence of the indicated concentration of Kapβ2 (5μM), Kapβ2$^{W460A:W730A}$ (5μM), or Impα (5μM) plus Kapβ1 (5μM). To determine the half maximal inhibitory concentration (IC$_{50}$), Kapβ2 was titrated into the above fibrillization reactions from 0.1-20μM. In some reactions, Ran^{Q69L}-GDP or Ran^{Q69L}-GTP (25μM) was also present, in which case GDP or GTP (1mM) were also present. In some FUS fibrillization reactions, HDAC1 (5μM or 50μM) or anti-FUS rabbit polyclonal antibody (NB100-562, Novus; 5μM) was also included.

Seeded fibril assembly—Figures 2 and S2

For 'seeded' assembly reactions, RBP fibrils were freshly prepared for each experiment. Fibril formation was confirmed by EM. These fibrils termed 'seed' were added at 5% (wt/wt) at the beginning of the fibrillization reaction. In this study, we only conducted self-seeding reactions, i.e., the primary sequence of the soluble RBP and fibrillar RBP were the same. FUS tends to form large tangles of fibrils, which must be dispersed prior to seeding reactions. Thus, FUS fibrils were formed for 3h as above, and then to separate fibrils an equal volume of high salt buffer (40mM HEPES-KOH, pH 7.4, 500mM KCl, 20mM MgCl$_2$, 10% glycerol, and 1mM DTT) was added and the incubation was continued for 2h. Seeded assembly reactions were performed as above for spontaneous fibrillization except that seeded reactions were not agitated. For experiments in Figure 2H, FUS seeding reactions were incubated at 25°C for 20min, TAF15, EWSR1, hnRNPA2, and TDP-43 seeding reactions were incubated at 25°C for 2h, and hnRNPA1 seeding reactions were incubated at 25°C for 4h. At the end of these seeded fibrillization reactions, minimal fibrillization occurred in the absence of added seed, whereas ∼20%–50% of RBP was in the aggregated state in the presence of seed 5% (wt/wt). Seeded fibrillization reactions were performed in the presence or absence of the indicated concentration of Kapβ2 (5μM), Kapβ2$^{W460A:W730A}$ (5μM), or Impα (5μM) plus Kapβ1 (5μM).

Turbidity was used to assess spontaneous and seeded fibrillization by measuring absorbance at 395nm. The absorbance was then normalized to that of WT RBP plus buffer control to determine the relative extent of aggregation. Alternatively, sedimentation analysis was used to assess spontaneous and seeded fibrillization. Thus, reactions were centrifuged at 16,100 g for 10 min at 4°C. Supernatant and pellet fractions were then resolved by sodium dodecyl sulfate polyacrylamide gel electrophoresis (SDS–PAGE) and stained with Coomassie Brilliant Blue or processed for immunoblot, and the amount in either fraction (% total) was determined by densitometry in comparison to known quantities of the RBP in question. For electron microscopy, fibrillization reactions (10 μl) were adsorbed onto glow-discharged 300-mesh Formvar/carbon coated copper grids (Electron Microscopy Sciences) and stained with 2% (w/v)

aqueous uranyl acetate. Excess liquid was removed, and grids were allowed to air dry. Samples were viewed by a JEOL 1010 transmission electron microscope.

Fibril disassembly—Figures 3 and S3

RBP fibrils were generated as above via spontaneous fibrillization and used for disassembly reactions. Preformed FUS (or FUS$^{\Delta NLS}$ or disease-linked FUS variant), TAF15 (or TAF15$^{\Delta NLS}$ or disease-linked TAF15 variant), or EWSR1 (or EWSR1$^{\Delta NLS}$ or disease-linked EWSR1 variant) fibrils (5μM monomer) were incubated at 25°C with Kapβ2 (5μM), Kapβ2$^{W460A:W730A}$ (5μM), or Impα (5μM) plus Kapβ1 (5μM) in the absence or presence of Ran^{GDP} or Ran^{GTP} (25μM) for 0-60min (Figures 3A–3F, S3A–S3C, and S3H). In other experiments, FUS fibrils (5μM monomer) were incubated at 25°C with Kapβ2 (5μM), HDAC1 (5 or 50μM), or anti-FUS antibody (5μM) for 0-60min (Figure 3H). Alternatively, FUS, TAF15, or EWSR1 fibrils (5μM monomer) were incubated at 25°C with Hsp104 (5μM) plus Sse1 (a yeast Hsp110; 1μM), Ssa1 (a yeast Hsp70; 1μM), and Ydj1 (a yeast Hsp40; 1μM), Hsp104^{A503S} (5μM) plus Sse1 (1μM), Ssa1 (1μM), and Ydj1 (1μM), or human Hsp110 (Apg2; 5μM), human Hsp70 (Hsc70; 5μM), and human Hsp40 (Hdj1; 5μM) for 0-60min (Figures S3D–S3F). TDP-43 fibrils (5μM monomer) were incubated at 25°C with Kapβ2 (5μM), Hsp104^{A503S} (5μM) plus Sse1 (an Hsp110; 1μM), Ssa1 (an Hsp70; 1μM), and Ydj1 (an Hsp40; 1μM), or Impα (5μM) plus Kapβ1 (5μM) for 0-60min (Figure 3J). In other experiments. TDP-43^{Q331K} or TDP-43$^{188-414}$ fibrils (5μM monomer) were incubated at 25°C with Kapβ2 (5μM), Kapβ2$^{W460A:W730A}$ (5μM), or Impα (5μM) plus Kapβ1 (5μM) for 0-60min (Figures S3I and S3J). Preformed hnRNPA1, hnRNPA1^{D262V}, hnRNPA1^{D262N}, or hnRNPA1$^{\Delta NLS}$ fibrils (5μM monomer) were incubated at 25°C with Kapβ2 (5μM) or Kapβ2$^{W460A:W730A}$ (5μM) for 0-72h (Figures 3L and 3M). For reactions containing Hsp104 or Hsp110, MgCl$_2$ (20mM), ATP (5mM), and an ATP regeneration system comprised of creatine kinase (0.2mg/ml) and creatine phosphate (10mM) were also added. Fibril disaggregation was performed without agitation and was assessed by turbidity, sedimentation analysis, and EM as described above. To determine the half maximal inhibitory concentration (EC$_{50}$), Kapβ2 was titrated into the above fibril disassembly reactions from 0-20μM (Figure 3G). For experiments in Figure 3I, Kapβ2 was biotinylated with Sulfo-NHS-LC-Biotin (Thermofisher) to achieve ~1-2 biotin moieties per Kapβ2. Biotinylated Kapβ2 (bio-Kapβ2) retained maximal disaggregase activity. His-FUS fibrils (5μM monomer) were disassembled with bio-Kapβ2 (5μM) for 2h. Neither the His-tag on FUS nor the biotin on Kapβ2 affected the ability of Kapβ2 to disaggregate FUS fibrils. The soluble disaggregation products were then recovered and incubated with Ran^{GDP} or Ran^{GTP} (25μM) for 30min. Soluble disaggregated products in the supernatant fraction were then depleted of bio-Kapβ2 using Pierce NeutrAvidin UltraLink Resin (Thermofisher) or His-FUS using Ni-NTA agarose (QIAGEN) in the presence or absence of Ran^{GDP} or Ran^{GTP} (25μM).

Luciferase disaggregation and reactivation—Figure S3G

Luciferase disaggregation and reactivation was performed as described previously (Jackrel et al., 2014). Chemically denatured firefly luciferase aggregates (50nM monomer) were incubated at 25°C for 90min with Kapβ2 (5μM), Hsp104 (5μM) plus Sse1 (1μM), Ssa1 (1μM), and Ydj1 (1μM), Hsp104^{A503S} (5μM) plus Sse1 (1μM), Ssa1 (1μM), and Ydj1 (1μM), or Hsp110 (Apg2; 5μM), Hsp70 (Hsc70; 5μM), and Hsp40 (Hdj1; 5μM). Luciferase reactivation was then determined.

Liquid droplet formation and disassembly—Figure S4

FUS liquid droplets were formed by incubating GST-TEV-FUS (10μM) in the presence or absence of Kapβ2 or Kapβ2$^{W460A:W730A}$ (10μM) in FUS assembly buffer (50mM Tris-HCl, pH 8, 200mM trehalose, 1mM DTT, and 20mM glutathione) for 4 hr at 25°C. Protein samples were then spotted onto a coverslip and imaged by Differential interference contrast (DIC) microscopy. In disassembly experiments, GST-TEV-FUS droplets or GST-TEV-FUS^{P525L} (10μM monomer) were first formed via incubation for 4 hr at 25°C. Preformed droplets were then incubated with Kapβ2 or Kapβ2$^{W460A:W730A}$ (10μM) for 3min at 25°C and monitored by DIC microscopy.

Viscous hnRNPA1 liquids were formed by incubating GST-hnRNPA1 (~200mg/ml) in 40mM HEPES-NaOH, pH 7.4, 150mM NaCl, 5% glycerol, and 20mM glutathione on ice for 1h. Viscous GST-hnRNPA1 liquids were incubated with the indicated amount of Kapβ2 or Kapβ2$^{W460A:W730A}$ at 4°C for 6 hr before being photographed.

Hydrogel formation—Figure 4

To generate hydrogels, GST-FUS$^{1-214}$ (~60mg/ml) in 20mM Tris-HCl, pH 7.5, 500mM NaCl, 20mM β-mercaptoethanol, 0.1mM PMSF, and 10mM glutathione was incubated on ice for at least one week. GST-FUS (~20-40mg/ml) in 50mM Tris-HCl, pH 8, 200mM trehalose, and 20mM glutathione was incubated on ice for at least one month to form hydrogels. GST-hnRNPA1 (~200mg/ml) in 40mM HEPES-NaOH, pH 7.4, 150mM NaCl, 5% glycerol, and 20mM glutathione was incubated on ice for at least one month to form hydrogels. GST-hnRNPA1^{D262V} (~33mg/ml) in 40mM HEPES-NaOH, pH 7.4, 150mM NaCl, 5% glycerol, and 20mM glutathione was incubated on ice for 24 hr to for hydrogels. For EM, the hydrogel samples were prepared following the same protocol as above but in the cold room. Hydrogels were also removed from tubes and stood on the benchtop for photography.

Hydrogel disassembly—Figure 4

All hydrogels were stored at 4°C until use. Buffer (20mM Imidazole, pH 6.5, 232mM NaCl, 1mM EDTA, 2mM DTT, and 20% glycerol), Kapβ2, Kapβ2$^{W460A:W730A}$, or GFP was added on top of the hydrogel (40μl). FUS hydrogels (240μM monomer, 40μl) at the bottom of a PCR tube were treated for 0-20h at 25°C with buffer, Kapβ2 (54μM monomer, 100μl), or Kapβ2$^{W460A:W730A}$ (45μM monomer, 120μl) to give a molar ratio of Kapβ2/Kapβ2$^{W460A:W730A}$:FUS = 0.563. In other experiments, FUS hydrogels (629μM monomer, 40μl) were

treated for 20h at 25°C with buffer or Kapβ2$^{W460A:W730A}$ (87μM, 120μl) to give a molar ratio of Kapβ2$^{W460A:W730A}$:FUS = 0.415. FUS$^{1-214}$ hydrogels (1.3mM, 40μl) at the bottom of a PCR tube were treated for 20h at 25°C with Kapβ2 (78μM, 100μl) to give a molar ratio of Kapβ2:FUS$^{1-214}$ = 0.15. hnRNPA1 gels (3.1mM, 40μl) were treated for 24h at 25°C with buffer, Kapβ2 (78μM, 200μl), or Kapβ2$^{W460A:W730A}$ (78μM, 200μl) to give a molar ratio of Kapβ2:hnRNPA1 = 0.13. In other experiments, hnRNPA1 gels (1.99mM, 40μl) were treated for 24h at 25°C with buffer or GFP (215μM, 100μl) to give a molar ratio of GFP:hnRNPA1 = 0.27. hnRNPA1^{D262V} gels (0.51mM, 40μl) were treated for 24h at 25°C with buffer or Kapβ2 (78μM, 200μl) to give a molar ratio of Kapβ2: hnRNPA1^{D262V} = 0.76. Finally, hnRNPA1$^{G274A:P288A:Y289A}$ gels (3mM, 40μl) were treated for 24h at 25°C with buffer or Kapβ2 (78μM, 200μl). Molar ratio of Kapβ2: hnRNPA1$^{G274A:P288A:Y289A}$ = 0.13. Samples were processed for photography, EM, or rheology (see below).

Rheology—Figures 4 and S4

For rheological measurements, the samples were separated into two phases by a short pulse spin, the top liquid phase was removed by pipetting and the bottom phase was used for rheology. For GST-FUS WT hydrogel, after adding Kapβ2 for 24 hr, only one phase is observed. Therefore, after the short pulse spin, 40μl sample was taken from the bottom of the tube for rheology measurements. The viscoelastic properties of each hydrogel were characterized by rheological measurements on an AR2000 rheometer (TA Instruments) using a cone–plate geometry (20mm diameter, 59min 42 s cone angle, and 27μm gap) (Rodell et al., 2013). To evaluate rheological properties, material responses to increasing strain were measured with oscillatory strain sweeps from 0.01 to 1000% strain at 1Hz. The frequency dependence of material properties to the application of strain were measured with oscillatory frequency sweeps from 0.01 to 100Hz at 0.5% strain. Reported storage modulus (G') and loss modulus (G") values were averaged value from 5-minute time sweeps at 4°C, 1Hz and 0.5% strain, corresponding to the plateau range of the hydrogels examined.

Yeast Procedures

Yeast procedures were performed according to standard protocols (Sun et al., 2011). We used the PEG/lithium acetate method to transform yeast with plasmid DNA. Yeast cells were grown in rich media (YPD) or in synthetic media lacking L-histidine and uracil and containing 2% glucose (SD/-His-Ura), raffinose (SRaf/-His-Ura), or galactose (SGal/-His-Ura). A Kapβ2 Gateway entry clone was generously provided by Gideon Dreyfuss containing full-length human Kapβ2 in pDONR221. A Gateway LR reaction was used to shuttle Kapβ2 into the Gateway-compatible yeast expression vector pAG413Gal-ccdB. A galactose-inducible GFP-FUS (pYES2CT/GFP-FUS) construct was generously provided by Gregory Petsko (Ju et al., 2011). A copper-inducible GFP-FUS (p426CUP-GFP-FUS) was also generated. QuikChange Site-Directed Mutagenesis Kit (Agilent) was used to generate mutant plasmids according to the manufacturer's instructions. Mutations were verified by DNA sequencing. The pAG413Gal-Kapβ2 and pYES2CT/GFP-FUS constructs were transformed into BY4741 (*MATa his3 leu2 met15 ura3*).

Yeast Western Blotting—Figures S5A and S5B

Yeast lysates were extracted after incubation with 0.2M NaOH at room temperature for 5 min. Lysates were then subjected to Tris-HCl SDS-PAGE (4%–20% gradient, Bio-Rad) and transferred to a PVDF membrane (Millipore). Membranes were blocked in Odyssey Blocking Buffer (LI-COR) overnight at 4°C. Primary antibody incubations were performed at room temperature for 1-2 h. After washing with PBS+0.05% Tween 20 (PBST), membranes were incubated with fluorescently labeled secondary antibodies at room temperature for 1 h, followed by washing with PBST. Proteins were detected using an Odyssey Fc Dual-Mode Imaging system. Primary antibody dilutions were as follows: anti-Kapβ2 monoclonal antibody (Sigma-Aldrich), 1:5000; anti-FUS rabbit polyclonal antibody (Bethyl), 1:5000. Fluorescently labeled anti-mouse and anti-rabbit secondary antibodies were used at 1:5000.

Yeast Fluorescence Microscopy—Figures 5A–5D

For fluorescence microscopy experiments, yeast were grown to mid-log phase in SRaf/-His-Ura media at 30°C. Cultures were diluted to an OD600 of 0.4 in SGal/-His-Ura to induce expression of Kapβ2 or Kapβ2$^{W460A:W730A}$ and the indicated FUS, EWSR1, hnRNPA1, or hnRNPA2 variant. Cultures were induced with galactose for 4-6h before being stained with Hoechst dye to visualize nuclei and processed for microscopy (Sun et al., 2011). In some experiments, yeast were grown overnight at 30°C in SRaf/-His-Ura and then diluted to OD600 of 0.8 in SRaf/-His-Ura plus 20μM CuSO$_4$ to induce GFP-FUS for 2h at 30°C. Cells were then transferred to SGal/-His-Ura to induce Kapβ2 for 3h at 30°C. Cultures were then stained with Hoechst dye to visualize nuclei and processed for microscopy. Images were obtained using an Olympus IX70 inverted microscope and a Photometric CoolSnap HQ 12-bit CCD camera. Z stacks of several fields were collected for each strain. Representative cells were chosen for figures. At least 100 cells per sample were counted for each replicate.

HEK293T and HeLa Cell culture and transfection-Figures 5E–5H, S5, and S6

HEK293T and HeLa cells were grown in Dulbecco's modified Eagle's medium (DMEM) supplemented with 10% fetal bovine serum (FBS), 1% penicillin/streptomycin, and 1% L-glutamate. Cells were transfected using either Lipofectamine LTX with Plus Reagent (Invitrogen) or FuGENE 6 Transfection Reagent, according to the manufacturer's instructions.

Tracking Stress Granule Assembly in HeLa cells—Figures 5, 6, and S5

HeLa cells were transfected with GFP, GFP-tagged Kapβ2, GFP-tagged Kapβ2$^{W460A:W730A}$, or GFP-tagged Kapβ2^{TL} together with HA-tagged FUS. 24 hr post-transfection, cells were stimulated with 0.5mM sodium arsenite for the indicated time, and immuno-stained with anti-HA, anti-G3BP1 (or anti-eIF4G), and DAPI. The percentage of HA-FUS-positive SG containing cells was then calculated: (number of cells with HA-FUS-positive SGs/number of transfected cells) x 100. Cells with at least three HA-FUS-positive SGs (HA- and G3BP1 (or eIF4G)-positive puncta) are counted as 'cells with HA-FUS-positive SGs'. The area to count was randomly selected in each slide. Every transfected cell in the selected area was counted. In each experiment, ~100-300 cells per slide were counted. The results of three experiments were then averaged to calculate the % of cells with HA-FUS-positive SGs. These averaged numbers from separate experiments are used to calculate the SEM.

Immunofluorescence of HeLa cells-Figures 5, 6, and S5

HeLa cells were fixed in 4% paraformaldehyde in PBS buffer, permeabilized with 0.5% Triton X-100 in PBS for 10 min, blocked with 5% goat serum in PBS for 30 min and incubated with primary antibody for 2h at room temperature (20–25°C) or overnight at 4°C. Primary antibodies were visualized with secondary antibodies conjugated with Alexa Fluor 488 and Alexa Fluor 594 (Molecular Probes, Invitrogen) and nuclei were detected using DAPI. Stained cells were examined using a confocal microscope (Zeiss LSM 780) with Zeiss ZEN software.

Genome editing and culture of human neural progenitor cells—Figure S6

ReNcell VM human neural progenitors (Millipore #SCC008) (Choi et al., 2014; Kim et al., 2015) were CRISPR-edited to introduce the ALS-linked FUS^{R521H} mutation in the endogenous FUS gene following a protocol previously described (Ran et al., 2013). After CRISPR-editing, isogenic clones were sequenced to select individual clones carrying either wild-type or a homozygous R521H mutation in the *FUS* gene.

Isogenic neural progenitors were maintained in high-glucose DMEM/F12 (ThermoFisher Scientific) media supplemented with 2μg/ml heparin (StemCell Technologies, #07980), 2% (v/v) B27 neural supplement (ThermoFisher Scientific, #175004044), 20μg/ml hEGF (Sigma-Aldrich, #E9644), 20μg/ml bFGF (Stemgent, #03-0002) and 1% penicillin/streptomycin (ThermoFisher Scientific) and were plated onto Matrigel (BD Biosciences)-coated cell culture 24-well format coverslips. Nucleofection using Nucleofector kit (Lonza, #VPG 1005) was used for neural progenitor cells to achieve high efficiency of transfection of plasmids pCDNA3.1 GFP-Kapβ2, pCDNA3.1 GFP-Kapβ2$^{W460A:W730A}$, pGFPmax (Lonza). 24 hr after transfection, the cells were treated with or without 0.5mM sodium arsenite for 1 hr, and stress granule assembly was assessed as below.

24 hr after transfection, the human neural progenitors were fixed in 4% paraformaldehyde for 15 min and washed thrice with PBS. Cells were permeabilized with 0.1% Triton X-100 for 15 min at room temperature. They were washed thrice again with PBS and blocked with 1% bovine serum albumin and 2% donkey serum in PBS for 1 hr at room temperature. Cells were incubated with primary antibodies (anti-FUS, Proteintech 11570-1-AP, 1:200) in the blocking solution and incubated during 1h at room temperature. Rabbit fluorescently tagged secondary antibody conjugated to cy3 (Jackson Immunoresearch) was incubated for 1 hr at room temperature in the blocking solution. The nuclei were stained with DAPI (ThermoFisher #S33025) and mounted with ProLong Gold Antifade Mountant (ThermoFisher # P36934) on slides for confocal microscopy. Imaging was performed at 60X magnification using a Nikon eclipse Ti confocal fluorescence microscope system. Percentage of GFP-positive cells with FUS stress granules were counted by blinded investigators from three independent experiments.

Human Cell Toxicity—Figures 5 and S6

HEK293T cells were plated in 96-well format and transfected with FuGene (Roche) according to the manufacturer's instructions. After 72h post-transfection, MTT (3-(4,5-Dimethylthiazol-2-yl)- 2,5-diphenyltetrazolium bromide) (Sigma) was added. The cells were incubated with MTT for 3h at 37°C. Acidic Isoproponal (40mM HCl) was then added to each well to solubilize the blue formazan crystals. Absorbance of each well was read with a Tecan Safire II plate reader using 570nm for absorbance and 630nm as a reference wavelength. Absorbance measurements were normalized to the absorbance of untransfected cells and used to calculate a percent viability for each condition. Alternatively, toxicity was assessed via lactate dehydrogenase (LDH) release using CytoTox-ONE kit (Promega).

Lentivirus-mediated overexpression of Kapβ2 in human fibroblasts—Figure S6

Kapβ2 was subcloned into pinducer20 plasmid (Addgene #44012). Lentivirus expressing Kapβ2 was generated at $6.75x10^9$ IU/mL by the MGH-Vector Core (Charlestown, MA, USA). Immortalized fibroblasts were plated in 6-well format. The fibroblasts were infected 24 hr after plating with $34x10^6$ IU/ml and 10μg/ml of polybrene (Santa Cruz Biotechnology). 72 hr after infection, the Kapβ2 transgene was induced by doxycycline (Sigma) at 1μg/ml for 72 hr.

RNA Isolation and Expression Analysis—Figure S6

Total RNA was isolated from control and ALS-FUS mutant fibroblasts using Trizol reagent (ThermoFisher Scientific). Using a Reverse Transcriptase kit (ThermoFisher #4374966), 300ng of total RNA was reverse transcribed to generate cDNA. Real-time quantitative PCR was performed to determine the expression levels of Kapβ2 after lentiviral induction. The expression levels of 3 mRNAs

downregulated in fibroblasts from FUS-R521H ALS patients (TPST2, WNT5A, ITGA3) were determined by quantitative RT-PCR after 72h of Kapβ2 induction. Quantitative RT-PCR was carried out using the iTaq universal sybr green supermix kit (BioRad), one denaturation step at 95°C for 5 min, 45 cycles of amplification (95°C for 10 s, 58°C for 30 s), then 65°C for 5 s and a final step at 95°C for 50 s using the specific human primers for *RPLP0* (Forward: GAAGTCACTGTGCCAGCCCA, Reverse: GAAGGTGTAATCCGTCTCCA), for Kapβ2 (*TNPO1*) (Forward: TCCCTTTACTTGAGTGCCTATC; Reverse: TAGCATGGCTTGTGCAAGAG), for *TPST2* (Forward: CAAC AAGGACCCATTTACGCTC, Reverse: TACACAGGCAGGCACTTCTCC), for *WNT5A* (Forward: CATGAACCTGCACAACAAC, Reverse: AGCATGTCTTCAGGCTACAT) and for *ITGA3* (Forward: TGGCAGACCTACCACAACG, Reverse: CTGGCTCAGCAAGA ACACC).

Quantitative PCR in fly—Figure S7
7 fly heads from age-matched flies were collected per sample and RNA was purified from the fly heads using Trizol reagent. cDNA was derived from RNA by reverse transcription. Expression of the endogenous *Drosophila* Kapβ2 gene was measured using qPCR and normalized against the expression level of alpha-Tubulin-84b.

Kapβ2 primer sequence: 5′/56-FAM/CATTATCAA/ZEN/CCGCCCGAACACGC/3IABkFQ/3′; 5′GGAGACCAAGCAGTACATACG3′; 5′GCAAATAAGGAGCCACTTCAAC3′.

Alpha-Tubulin-84b primer sequence: 5′/56 FAM/TCACACGCG/Zen/ACAAGGAAAATTCACAGA/3IABkFQ/3′; 5′CCTCGAAATCG TAGCTCTACAC3′; 5′ACCAGCCTGACCAACATG3′. The qPCR data were analyzed using the statistics software package Graphpad Prism.

Drosophila eye images and quantification—Figure S7
The left eyes of 2-day old female flies were photographed using a Leica M205C stereomicroscope. Fly eye phenotypes were assessed using a quantitative scale in which points were assigned for the following criteria: disorder in the ommatidial array; ommatidial fusion; altered appearance of hairs between the ommatidia; loss of pigmentation; speckling or presence of individual ommatidia with obviously different pigmentation; increased reflectiveness of the eye surface; presence of necrotic patches; decreased size of the eye. For each criterion, points were assigned based on the extent of the abnormality. 10 flies were assessed for each genotype. For each separate experiment the control and experimental flies were assessed at the same time.

Drosophila lifespan experiments—Figure 5
OK371-HA-FUS[R521H] males were crossed with virgin females at 18°C, which ensures low expression of HA-FUS[R521H] and eclosion of adult flies. The OK371-HA-FUS-R521H strain must be maintained at 18°C or lower to be viable. F1 progeny females were collected on the day of eclosion and placed at 28°C for lifespan measurements.

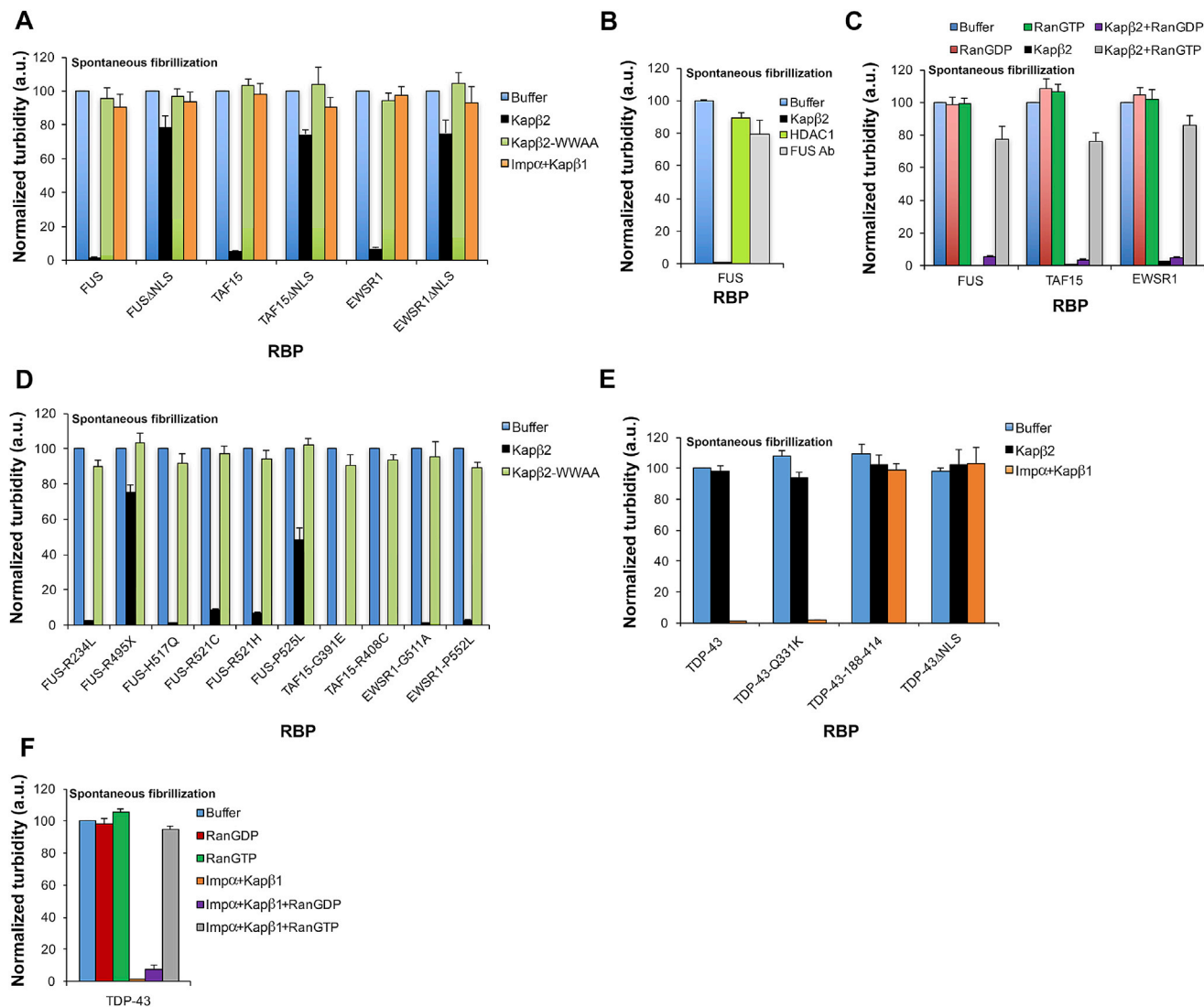### Adult fly muscle preparation and immunohistochemistry—Figure 7
For immunostaining of indirect flight muscles, female flies were used because they have a bigger thorax. Adult flies were embedded in a drop of OCT compound (Sakura Finetek) on a glass slide, frozen with liquid nitrogen and bisected sagitally by a razor blade. After fixing with 4% paraformaldehyde in PBS, hemithoraces were stained by Texas Red-X phalloidin (Invitrogen) and DAPI according to manufacturer's instructions. Stained hemi-thoraces were mounted in 80% glycerol, and the musculature was examined by DMIRE2 (Leica, 103). For hnRNPA2 staining, hemithoraces were permeabilized with PBS containing 0.2% Triton X-100 and stained with anti-hnRNPA2B1 (EF-67) antibody (Santa Cruz Biotechnology) and Alexa 488-conjugated secondary antibody (Invitrogen). Stained muscle fibers were dissected and mounted in Fluormount-G (Southern Biotech) and imaged with a Marianas confocal microscope (Zeiss, 363).

Fly western blotting—Figures 7 and S7
For western blot, male and female flies were used with 1:1 ratio. Thoraces of adult flies were prepared and ground in PBS containing 0.2% Triton X-100. After adding SDS sample buffer, samples were boiled for 5 min and analyzed by the standard western blotting method provided by Odyssey system (LI-COR) with 4%–12% NuPAGE Bis-Tris Gel (Invitrogen) and anti-hnRNPA2B1 antibody (Santa Cruz, 1:1,000).

QUANTIFICATION AND STATISTICAL ANALYSIS

Statistical parameters including the definitions and exact values of n (e.g., number of biological repeats, number of flies, number of cells, etc), distributions and deviations are reported in the Figures and corresponding Figure Legends (or STAR Methods section). p > 0.05, not significant, *p < 0.05, **p < 0.01 and ***p < 0.001 by Student's t test, one-way ANOVA, two-way ANOVA or Log-rank test. Dunnett or Bonferroni correction were used in ANOVA to control family-wise error rate of the tested simple effects, separately per level of the second factor (e.g., time point) in two-way ANOVA. Statistical analysis was performed in GraphPad Prism or Excel.

Figure S1. Kapβ2 Is a Potent Molecular Chaperone for Diverse RBPs with a PY-NLS, Related to Figure 1

(A) FUS, FUS$^{\Delta NLS}$, TAF15, TAF15$^{\Delta NLS}$, EWSR1, or EWSR1$^{\Delta NLS}$ (5μM) were incubated in the absence or presence of Kapβ2 (5μM), Kapβ2$^{W460A:W730A}$ (5μM), or Impα (5μM) plus Kapβ1 (5μM). Fibrillization was assessed after 90 min without agitation (FUS, FUS$^{\Delta NLS}$) or after 90min with agitation at 700rpm (TAF15, TAF15$^{\Delta NLS}$, EWSR1, or EWSR1$^{\Delta NLS}$) by turbidity. Values represent means ± SEM (n = 3).

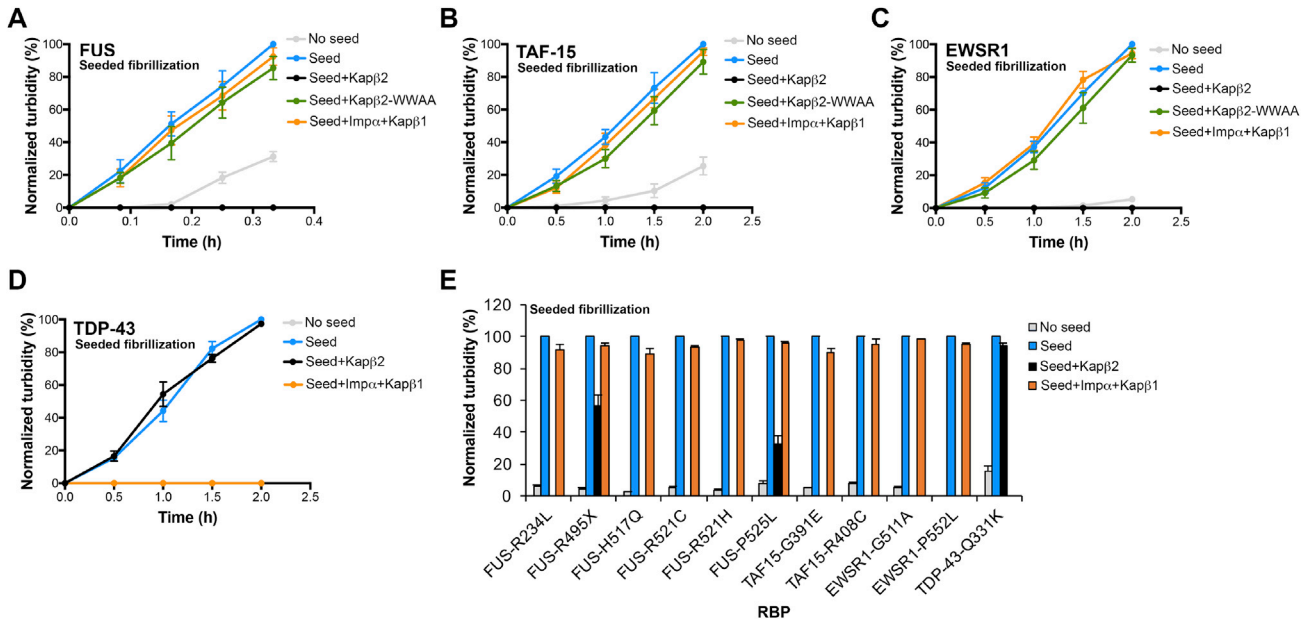(B) FUS (5μM) was incubated at 25°C for 90min without agitation in the absence or presence of Kapβ2 (5μM), HDAC1 (5μM) or anti-FUS antibody (5μM). Fibrillization was assessed by turbidity. Values represent means ± SEM (n = 3).

(C) FUS, TAF15, or EWSR1 (5μM) were incubated as in (A) in the absence or presence of Kapβ2 (5μM) plus or minus Ran^{GDP} or Ran^{GTP} (25μM). Fibrillization was assessed by turbidity. Values represent means ± SEM (n = 3).

(D) FUS^{R234L}, FUS^{R495X}, FUS^{H517Q}, FUS^{R521C}, FUS^{R521H}, FUS^{P525L}, TAF15^{G391E}, TAF15^{R408C}, EWSR1^{G511A}, or EWSR1^{P552L} (5μM) were incubated as in (A) in the absence or presence of Kapβ2 (5μM) or Kapβ2$^{W460A:W730A}$ (5μM). Fibrillization was assessed by turbidity. Values represent means ± SEM (n = 3).

(E) TDP-43, TDP-43^{Q331K}, TDP-43$^{188-414}$ or TDP-43$^{\Delta NLS}$ (5μM) were incubated at 25°C for 90min with agitation at 700rpm (TDP-43, TDP-43^{Q331K}, and TDP-43$^{188-414}$) or 16h with agitation at 700rpm (TDP-43$^{\Delta NLS}$) in the absence or presence of Kapβ2 (5μM) or Impα (5μM) plus Kapβ1 (5μM). Fibrillization was assessed by turbidity. Values represent means ± SEM (n = 3).

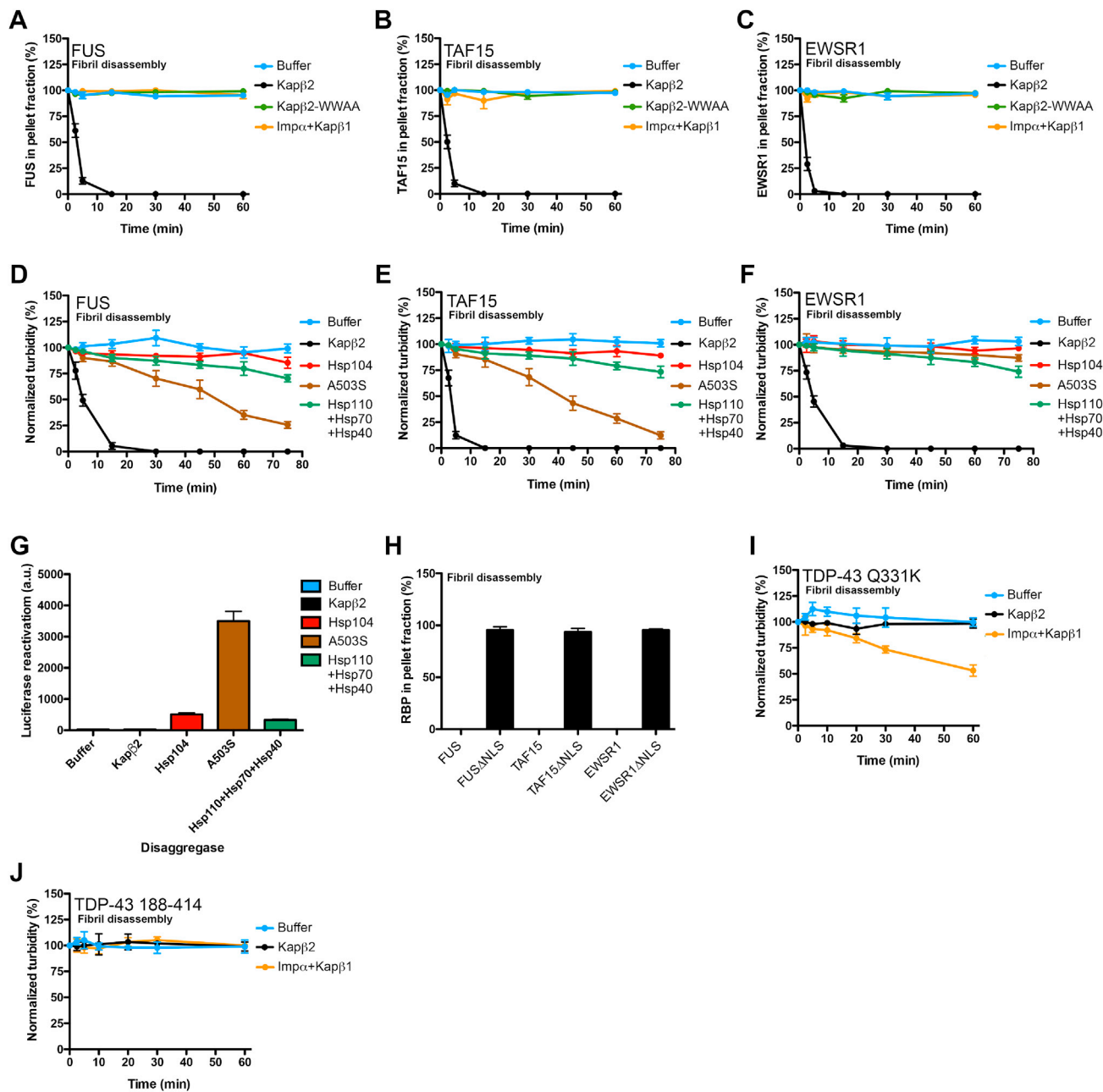(F) TDP-43 (5μM) was incubated as in (E) in the absence or presence of Impα (5μM) and Kapβ1 (5μM) plus or minus Ran^{GDP} or Ran^{GTP} (25μM). Fibrillization was assessed by turbidity. Values represent means ± SEM (n = 3).

Figure S2. Kapβ2 Inhibits Seeded Fibril Assembly of Diverse RBPs with a PY-NLS, Related to Figure 2

(A–D) (A) FUS (5μM) plus or minus preformed FUS fibrils (5% wt/wt), (B) TAF15 (5μM) plus or minus preformed TAF15 fibrils (5% wt/wt), (C) EWSR1 (5μM) plus or minus preformed EWSR1 fibrils (5% wt/wt), or (D) TDP-43 (5μM) plus or minus preformed TDP-43 fibrils (5% wt/wt) were incubated at 25°C without agitation for the indicated time in the absence or presence of Kapβ2 (5μM), Kapβ2$^{W460A:W730A}$ (5μM), or Impα (5μM) plus Kapβ1 (5μM). Fibrillization was assessed by turbidity. Values represent means ± SEM (n = 3).

(E) The indicated disease-linked RBP (5μM) plus or minus preformed fibrils of the same disease-linked RBP (5% wt/wt) was incubated at 25°C without agitation in the absence or presence of equimolar Kapβ2 (5μM) or Impα (5μM) plus Kapβ1 (5μM). Fibrillization was assessed by turbidity after 15min for FUS variants and 1.5h for TAF15, EWSR1, and TDP-43 variants. Values represent means ± SEM (n = 3).

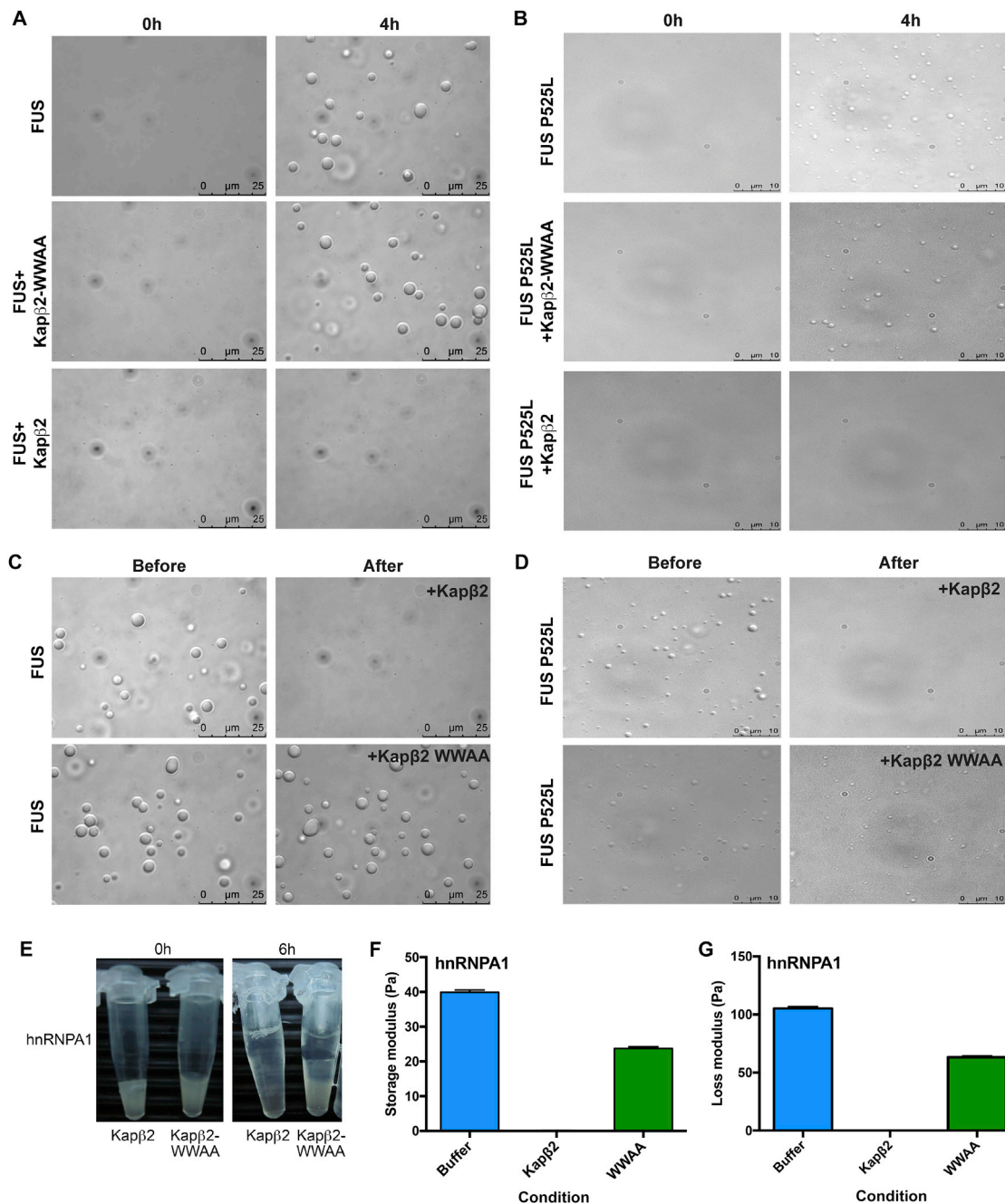**Figure S3. Kapβ2 Disaggregates Preformed Fibrils of Diverse RBPs with a PY-NLS, Related to Figure 3**

(A–C) Preformed FUS (A), TAF15 (B), or EWSR1 (C) fibrils (5μM monomer) were incubated at 25°C with Kapβ2 (5μM), Kapβ2[W460A:W730A] (5μM), or Impα (5μM) plus Kapβ1 (5μM) for 0-60min. Disaggregation was assessed by sedimentation analysis. Values represent means ± SEM (n = 3).
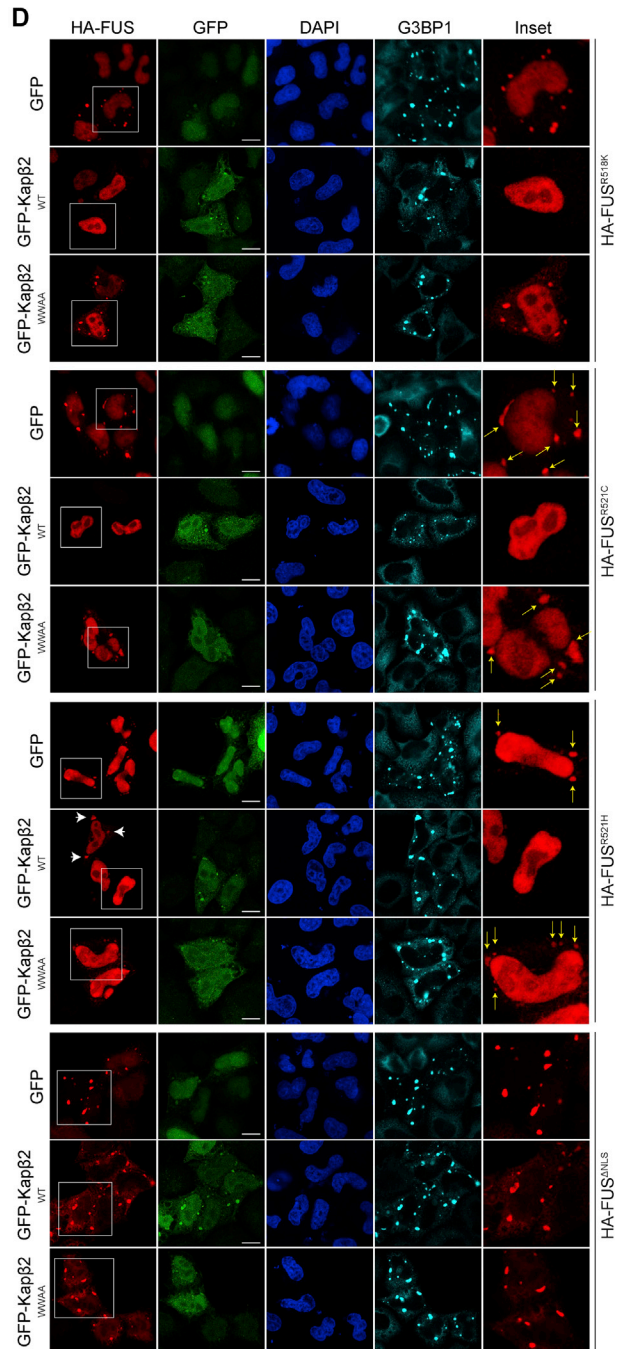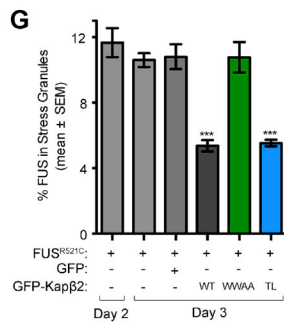
(D–F) Preformed FUS (D), TAF15 (E), or EWSR1 (F) fibrils (5μM monomer) were incubated at 25°C with Kapβ2 (5μM), Hsp104 (5μM) plus Sse1 (1μM), Ssa1 (1μM), and Ydj1 (1μM), Hsp104[A503S] (5μM) plus Sse1 (1μM), Ssa1 (1μM), and Ydj1 (1μM), or Hsp110 (Apg2; 5μM), Hsp70 (Hsc70; 5μM), and Hsp40 (Hdj1; 5μM) for 0-60min. Disaggregation was assessed by turbidity. Values represent means ± SEM (n = 3).

(G) Chemically denatured firefly luciferase aggregates (50nM monomer) were incubated at 25°C for 90min with Kapβ2 (5μM), Hsp104 (5μM) plus Sse1 (1μM), Ssa1 (1μM), and Ydj1 (1μM), Hsp104[A503S] (5μM) plus Sse1 (1μM), Ssa1 (1μM), and Ydj1 (1μM), or Hsp110 (Apg2; 5μM), Hsp70 (Hsc70; 5μM), and Hsp40 (Hdj1; 5μM). Luciferase reactivation was then determined. Values represent means ± SEM (n = 3).

(H) Preformed fibrils of the indicated RBP (5μM monomer) were incubated at 25°C with Kapβ2 (5μM) for 60min. Disaggregation was assessed by sedimentation analysis. Values represent means ± SEM (n = 3).

(I and J) Preformed TDP-43[Q331K] (I) or TDP-43[188-414] (J) fibrils (5μM monomer) were incubated at 25°C with Kapβ2 (5μM), Kapβ2[W460A:W730A] (5μM), or Impα (5μM) plus Kapβ1 (5μM) for 0-60min. Disaggregation was assessed by turbidity. Values represent means ± SEM (n = 3).

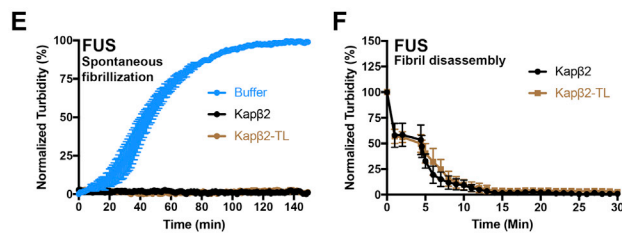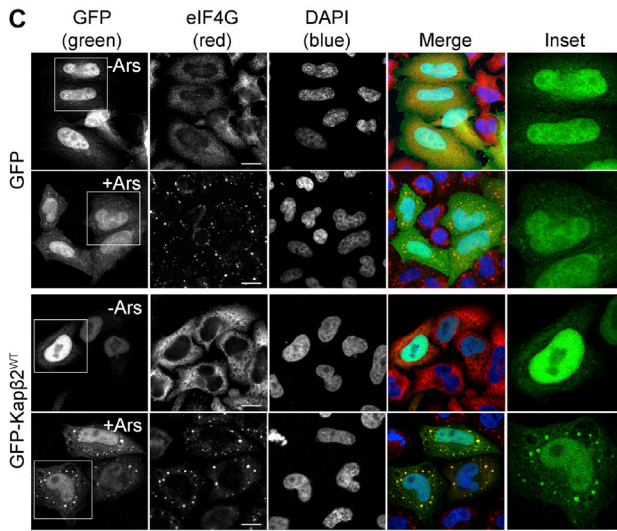**Figure S4. Kapβ2 Rapidly Disperses Liquid Droplets Formed by FUS and hnRNPA1, Related to Figure 4**

(A and B) GST-TEV-FUS (A) or GST-TEV-FUS[P525L] (B) (10μM) was incubated at 25°C for 4h in the presence or absence of Kapβ2 or Kapβ2[W460A:W730A] (10μM). Protein samples were then spotted onto a coverslip and imaged by DIC microscopy. Scale bar is 25μm (A) and 10μm (B).

(C and D) GST-TEV-FUS droplets (C) or GST-TEV-FUS[P525L] (D) (10μM monomer) were incubated with Kapβ2 or Kapβ2[W460A:W730A] (10μM) for 3min at 25°C and monitored by DIC microscopy. Scale bar is 25μm (A) and 10μm (B).

(E) A viscous hnRNPA1 liquid phase (3.3mM, 40μl) rapidly assembles at 4°C and accumulates at the bottom of a PCR tube. Addition of Kapβ2 (78μM, 100μl) but not Kapβ2[W460A:W730A] (78μM, 100μl) dissolves these viscous hnRNPA1 liquids after 6h at 4°C. Molar ratio of Kapβ2: hnRNPA1 = 0.06.

(F and G) Rheology was employed to determine the storage modulus (F) and loss modulus (G) of viscous hnRNPA1 liquid phase (3.3mM, 40μl) treated with buffer or Kapβ2 (78μM, 200μl) or Kapβ2[W460A:W730A] (78μM, 100μl). Molar ratio of Kapβ2: hnRNPA1[D262V] = 0.06. Values represent means ± SEM.

(legend on next page)

Figure S5. Kapβ2 Localizes to Stress Granules, Antagonizes Incorporation of FUS into Stress Granules, and Reduces Cell Toxicity, Related to Figure 5

(A) Yeast cells coexpressing the indicated GFP-tagged RBP and vector, Kapβ2, or Kapβ2$^{W460A:W730A}$ were processed for immunoblot. 3-Phosphoglycerate kinase (PGK) serves as a loading control.

(B) Yeast cells expressing GFP-FUS from the copper promoter for 2h were processed for immunoblot (left panels) or shifted to galactose media without copper for 3h to induce Kapβ2 or Kapβ2$^{W460A:W730A}$ expression and switch off FUS expression and processed for immunoblot (right panels). 3-Phosphoglycerate kinase (PGK) serves as a loading control.
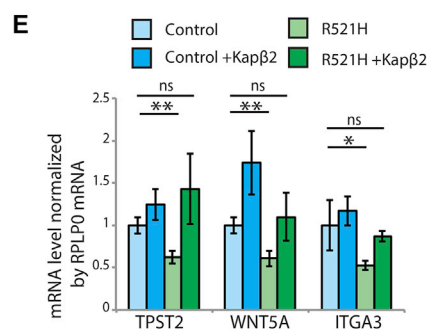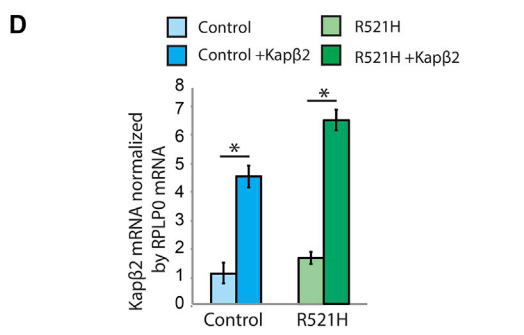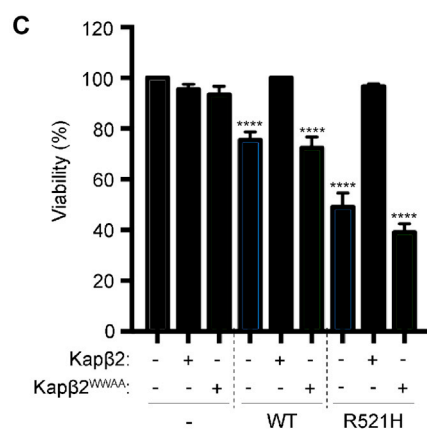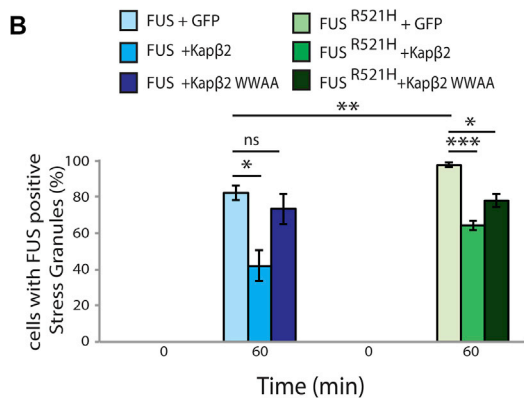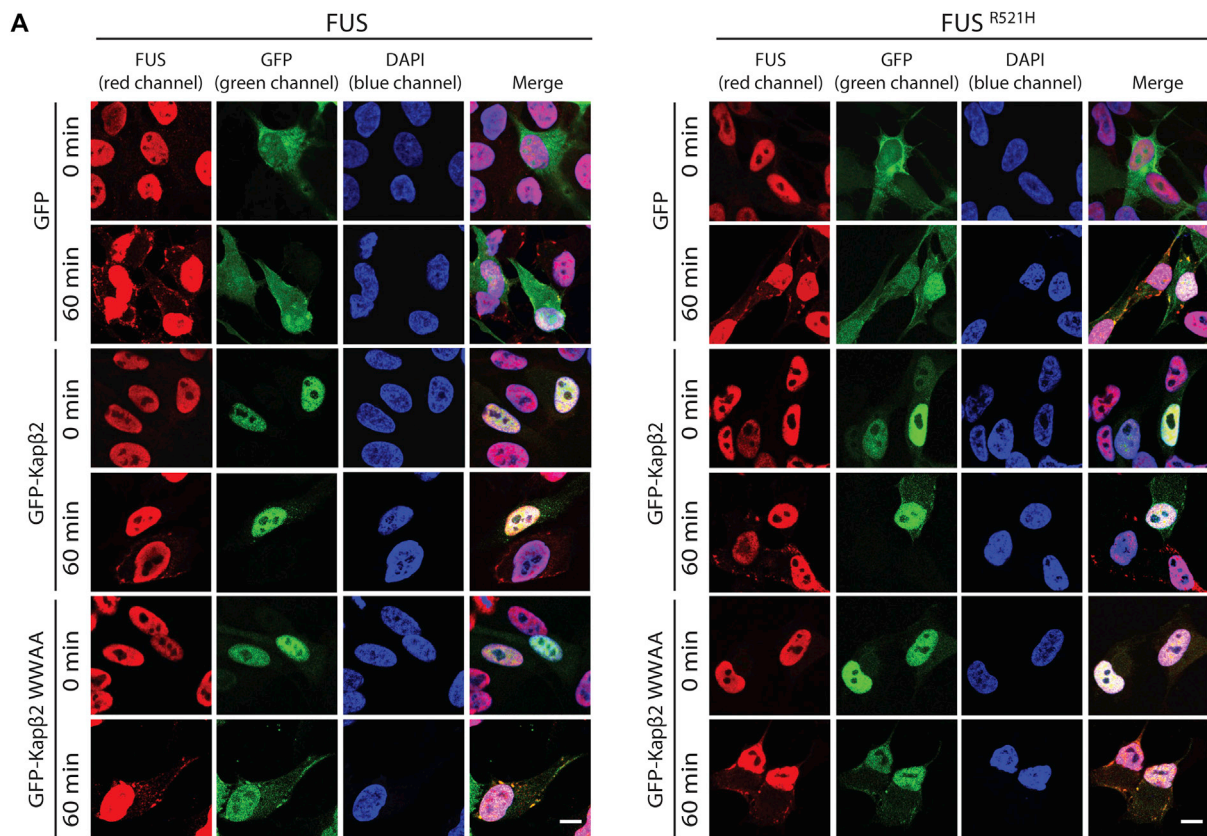
(C) HeLa cells were transfected with GFP or GFP-tagged Kapβ2. 24 hr post-transfection, cells were stimulated with 0.5mM sodium arsenite for 60 min, and immunostained with anti-eIF4G (red) and DAPI (blue). Cells at pre- (-Ars) and 60 min post-arsenite treatment (+Ars) are shown. Note that Kapβ2 gets incorporated into stress granules post-arsenite treatment. Scale bar, 10 μm.

(D) HeLa cells were transfected with GFP or GFP-tagged Kapβ2 together with HA-tagged FUS^{R518K}, HA-tagged FUS^{R521C}, HA-tagged FUS^{R521H} or HA-tagged FUS$^{\Delta NLS}$. 24 hr post-transfection, cells were fixed and immunostained with anti-HA, anti-G3BP1 and DAPI. Yellow arrows indicate FUS-positive stress granules. Arrowheads indicated FUS-positive stress granules in a neighboring cell that does not express GFP-Kapβ2^{WT}. Scale bar, 10 μm.

(E) FUS (5μM) was incubated in the absence or presence of Kapβ2 (5μM) or Kapβ2^{TL} (5μM) for 0-157 min at 25°C. Fibrillization was assessed by turbidity. Values represent means ± SEM (n = 3).

(F) Preformed FUS fibrils (5μM monomer) were incubated with Kapβ2 (5μM) or Kapβ2^{TL} (5μM) for 0-30 min at 25°C. Disaggregation was assessed by turbidity. Values represent means ± SEM (n = 3).

(G) HeLa cells were transfected with HA-FUS^{R521C} (Day 1). On the next day (Day 2), these cells were sequentially transfected with GFP or GFP-tagged Kapβ2 as indicated. 24 hr post-transfection (Day 3), cells were fixed and immunostained with anti-HA, anti-G3BP1, and DAPI. The percentage of transfected cells with FUS-positive stress granules is plotted. ***p < 0.001 by one-way ANOVA, Dunnett's multiple comparisons test. Values represents the means ± SEM (n = 3-6).

A

FUS | FUS R521H

GFP — 0 min / 60 min
GFP-Kapβ2 — 0 min / 60 min
GFP-Kapβ2 WWAA — 0 min / 60 min

Columns: FUS (red channel), GFP (green channel), DAPI (blue channel), Merge

B

FUS + GFP, FUS +Kapβ2, FUS +Kapβ2 WWAA
FUS R521H + GFP, FUS R521H +Kapβ2, FUS R521H +Kapβ2 WWAA

y-axis: cells with FUS positive Stress Granules (%)
x-axis: Time (min)

C

y-axis: Viability (%)

Kapβ2: − + − | − + − | − + −
Kapβ2 WWAA: − − + | − − + | − − +
− | WT | R521H

D

Control, Control +Kapβ2, R521H, R521H +Kapβ2

y-axis: Kapβ2 mRNA normalized by RPLP0 mRNA
x-axis: Control, R521H

E

Control, Control +Kapβ2, R521H, R521H +Kapβ2

y-axis: mRNA level normalized by RPLP0 mRNA
x-axis: TPST2, WNT5A, ITGA3

(legend on next page)

Figure S6. Kapβ2 Antagonizes Incorporation of FUS into Stress Granules in Human Neural Progenitors and Restores Expression of Selected FUS mRNA Targets in ALS Patient Fibroblasts, Related to Figure 5
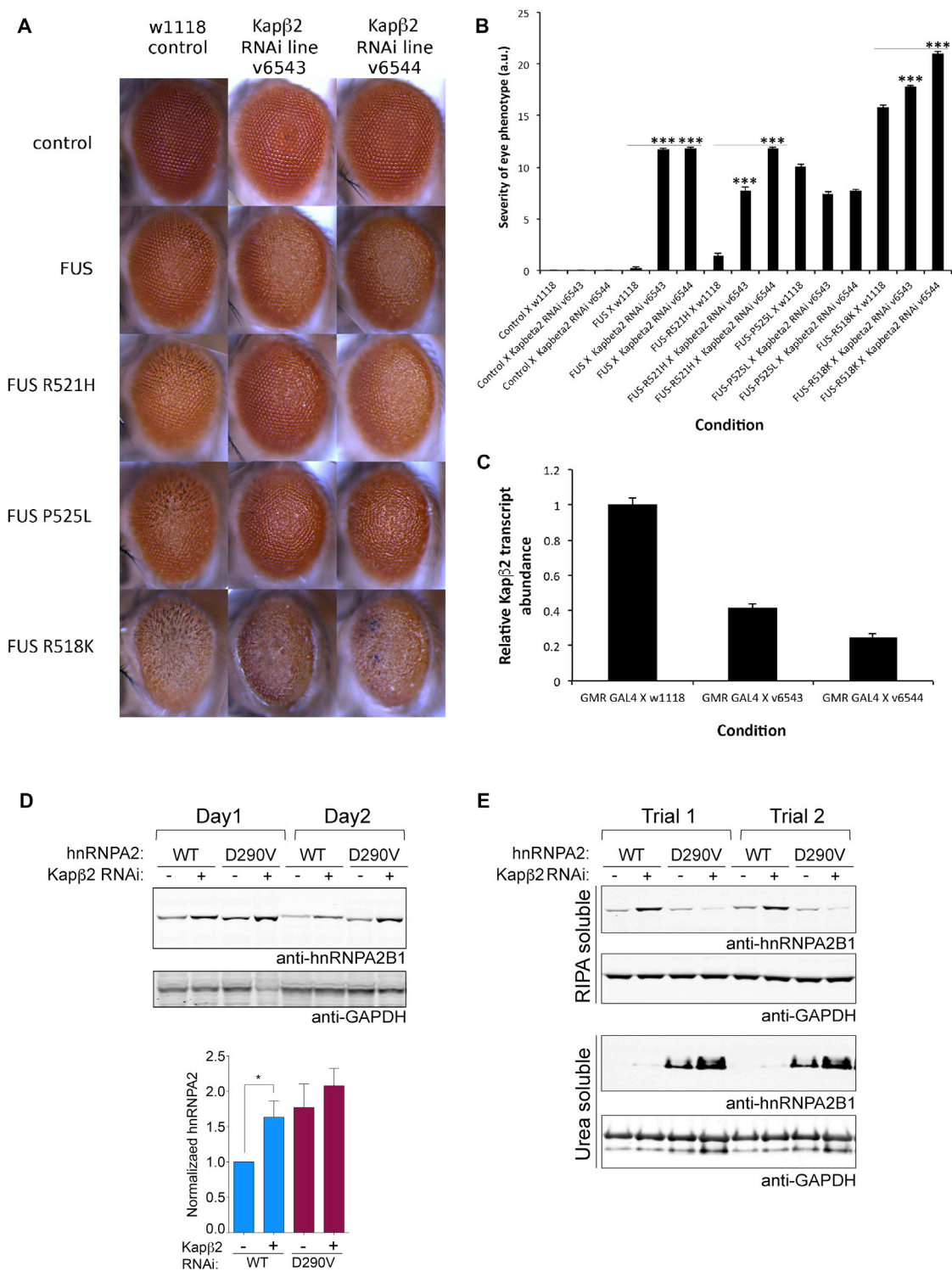
(A) Human neural progenitor cells edited with CRISPR/Cas9 to express endogenous wild-type or R521H mutant FUS were transfected with GFP, GFP-tagged Kapβ2 or GFP-tagged Kapβ2[W460A:W730A]. 24 hr post-transfection, cells were stimulated with 0.5 mM sodium arsenite for the indicated time, and immunostained with anti-FUS (red) and DAPI (blue). Scale bar, 10μm.

(B) Quantification of (A) to determine the percentage of GFP-positive human neural progenitor cells with FUS-positive cytoplasmic granules. Values represent means and error bars represent SEM from 3 independent experiments, 40-150 cells per condition. Student's t test, *, ** and *** indicate $p < 0.05$, $p < 0.01$ and $p < 0.001$, respectively.

(C) Kapβ2 but not Kapβ2[W460A:W730A] suppressed FUS and FUS[R521H] toxicity in human cells (HEK293T). Cell viability was assessed by LDH release assay. Values represent means ± SEM (n = 3). A one-way ANOVA with the post hoc Dunnett's multiple comparisons test was used to compare the control (no elevated FUS or Kapβ2 expression) to the other conditions **** denotes $p \leq 0.0001$.

(D) Quantitative RT-PCR analysis of Kapβ2 mRNA level normalized using the RPLP0 mRNA in 3 control and 3 patient FUS[R521H] fibroblast lines after 72h of lentiviral induction of Kapβ2 expression.

(E) Quantitative RT-PCR analysis of TPST2, WNT5A and ITGA3 mRNA levels in 3 control and 3 patient FUS[R521H] fibroblast lines after 72h of lentiviral induction of Kapβ2 expression. Values represent means and error bars indicate SEM of three biological replicates per condition (3 control lines and 3 patient lines). Student's t test, * and ** indicate $p < 0.05$ and $p < 0.01$, respectively. ns, non-significant.

A

| | w1118 control | Kapβ2 RNAi line v6543 | Kapβ2 RNAi line v6544 |

control

FUS

FUS R521H

FUS P525L

FUS R518K

B

Severity of eye phenotype (a.u.)

Condition

Control X w1118
Control X Kapbeta2 RNAi v6543
Control X Kapbeta2 RNAi v6544
FUS X w1118
FUS X Kapbeta2 RNAi v6543
FUS X Kapbeta2 RNAi v6544
FUS-R521H X w1118
FUS-R521H X Kapbeta2 RNAi v6543
FUS-R521H X Kapbeta2 RNAi v6544
FUS-P525L X w1118
FUS-P525L X Kapbeta2 RNAi v6543
FUS-P525L X Kapbeta2 RNAi v6544
FUS-R518K X w1118
FUS-R518K X Kapbeta2 RNAi v6543
FUS-R518K X Kapbeta2 RNAi v6544

C

Relative Kapβ2 transcript abundance

GMR GAL4 X w1118   GMR GAL4 X v6543   GMR GAL4 X v6544

Condition

D

	Day1		Day2	
hnRNPA2:	WT	D290V	WT	D290V
Kapβ2 RNAi:	- +	- +	- +	- +

anti-hnRNPA2B1

anti-GAPDH

Normalizaed hnRNPA2

| Kapβ2 RNAi: | - | + | - | + |
| | WT | | D290V | |

E

	Trial 1		Trial 2	
hnRNPA2:	WT	D290V	WT	D290V
Kapβ2 RNAi:	- +	- +	- +	- +

RIPA soluble

anti-hnRNPA2B1

anti-GAPDH

Urea soluble

anti-hnRNPA2B1

anti-GAPDH

Figure S7. Kapβ2 Knockdown Alters Disease-Linked RBP Toxicity, Stability, and Solubility in the Fly, Related to Figures 5 and 7

(A) Expression of FUS or ALS-linked FUS variants, FUS[R521H], FUS[P525L], or FUS[R518K] in fly eyes at 25°C causes a rough eye phenotype and neurodegeneration. This phenotype is most pronounced with FUS[R518K] and the least pronounced with FUS. Expression of siRNA for fly Kapβ2 in two independent lines (v6543 and v6544) enhances the rough eye phenotype of FUS, FUS[R521H], or FUS[R518K], but has minimal effect on FUS[P525L]. The rough eye phenotype of FUS[P525L] was not enhanced by Kapβ2 RNAi, which likely reflects the weaker binding of FUS[P525L] to Kapβ2 compared to FUS, FUS[R521H], and FUS[R518K].

(B) We performed quantification of eye phenotypes using previously published criteria and found that Kapβ2 knockdown enhanced the rough eye phenotype of FUS, FUS^{R521H}, or FUS^{R518K}, but has minimal effect on FUS^{P525L}. ***p < 0.001 by Mann-Whitney test.

(C) QPCR reveals that v6544 causes stronger depletion of Kapβ2. Correspondingly, v6544 produces stronger enhancement of the rough eye phenotype (A, B).

(D) Kapβ2 knockdown increases stability of hnRNPA2 in flies. Thoraces of adult flies were processed for western blot analysis with an antibody against hnRNPA2B1. GAPDH was blotted as a loading control. Quantification of hnRNPA2 levels on day 2 is shown in graph below. Values represent means ± SD (n = 3).

(E) Kapβ2 knockdown reduces solubility of hnRNPA2 in flies. Thoraces of adult flies were dissected and sequential extractions were performed to examine the solubility profile of hnRNPA2.